Antimicrobial peptides modulate lung injury by altering the intestinal microbiota

Ahmed Abdelgawad[1,3], Teodora Nicola[1,3], Isaac Martin[1], Brian A. Halloran[1], Kosuke Tanaka[1], Comfort Y. Adegboye[2], Pankaj Jain[1], Changchun Ren[1], Charitharth V. Lal[1], Namasivayam Ambalavanan[1], Amy E. O'Connell[2,4], Tamás Jilling[1,4], and Kent A. Willis[1,4,5*]

[1]Division of Neonatology, Department of Pediatrics, Heersink School of Medicine, University of Alabama at Birmingham, Birmingham, AL, USA
[2]Division of Newborn Medicine, Boston Children's Hospital; Department of Pediatrics, Harvard Medical School, Boston, MA, USA
[3]These authors contributed equally
[4]These authors contributed equally
[5]Lead Contact
*Correspondence: kawillis@uab.edu (K.W.)

SUMMARY
Mammalian mucosal barriers secrete antimicrobial peptides (AMPs) as critical host-derived regulators of the microbiota. However, mechanisms that support homeostasis of the microbiota in response to inflammatory stimuli such as supraphysiologic oxygen remain unclear. Here, we show that neonatal mice breathing supraphysiologic oxygen or direct exposure of intestinal organoids to supraphysiologic oxygen suppress the intestinal expression of AMPs and alters the composition of the intestinal microbiota. Oral supplementation of the prototypical AMP lysozyme to hyperoxia exposed neonatal mice reduced hyperoxia-induced alterations in their microbiota and was associated with decreased lung injury. Our results identify a gut-lung axis driven by intestinal AMP expression and mediated by the intestinal microbiota that is linked to lung injury. Together, these data support that intestinal AMPs modulate lung injury and repair.

INTRODUCTION
Fetal lung development is a tightly regulated process normally occurring at low oxygen tension[1]. However, premature birth exposes the developing lung to far greater oxygen levels and this is usually compounded by the clinical use of supplemental oxygen and mechanical ventilation after birth[2]. The direct effects of supraphysiologic oxygen on the lungs are well described[3], but there is also evidence for concurrent systemic, non-pulmonary oxygen toxicity exemplified by retinopathy of prematurity[3]. However, the effect of supraphysiologic oxygen on the host-microbiota interface of the neonatal intestine remains unclear.

Antimicrobial peptides (AMPs) are an extensive class of proteins secreted across mucosal surfaces that have central roles in the response to inflammation and the regulation of the commensal microbiota[4]. In addition to their antimicrobial properties, AMPs have anti-inflammatory, wound-healing, and tissue-protective effects[5]. In the newborn, intestinal and nasopharyngeal secretion of AMPs increases with age, potentially a necessary suppression to aid the establishment of a normal microbiota or to compensate for the intake of milk-derived AMPs[4]. Since AMP expression also increases in response to inflammation[5], supraphysiologic oxygen might disrupt initial microbial colonization.

While exploring the effects of hyperoxia exposure on the transcriptional landscape of the developing gut and lungs, we were intrigued by alterations in AMP production in the neonatal intestine that were

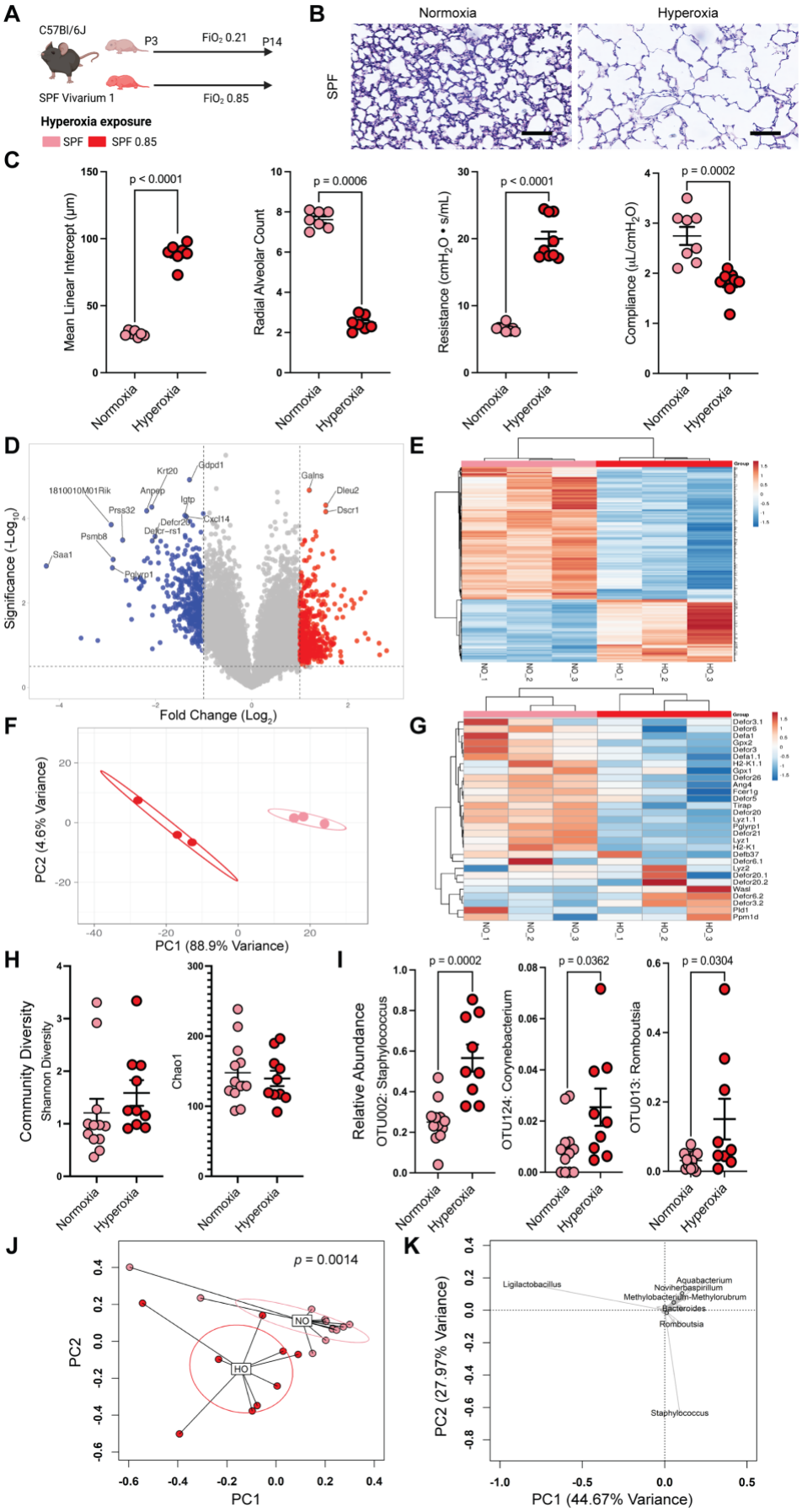
A
C57Bl/6J
P3
FiO2 0.21
P14
SPF Vivarium 1
FiO2 0.85
Hyperoxia exposure
SPF
SPF 0.85
B
Normoxia
Hyperoxia
SPF
C
Mean Linear Intercept (µm)
p < 0.0001
Radial Alveolar Count
p = 0.0006
Resistance (cmH2O • s/mL)
p < 0.0001
Compliance (µL/cmH2O)
p = 0.0002
Normoxia
Hyperoxia
D
Significance (-Log10)
Fold Change (Log2)
1810010M01Rik
Krt20
Gdpd1
Anpep
Igtp
Prss32
Defcr26
Cxcl14
Defcr-rs1
Psmb8
Saa1
Pglyrp1
Galns
Dleu2
Dscr1
E
F
PC2 (4.6% Variance)
PC1 (88.9% Variance)
G
H
Community Diversity
Shannon Diversity
Chao1
I
Relative Abundance
OTU002: Staphylococcus
p = 0.0002
OTU124: Corynebacterium
p = 0.0362
OTU013: Romboutsia
p = 0.0304
J
p = 0.0014
NO
HO
PC2
PC1
K
Ligilactobacillus
Aquabacterium
Noviherbaspirillum
Methylobacterium-Methylorubrum
Bacteroides
Romboutsia
Staphylococcus
PC2 (27.97% Variance)
PC1 (44.67% Variance)

Figure 1 (Preceding page). Oxygen exposure reduces intestinal antimicrobial peptide expression.
A) Neonatal C57BL/6J mice were exposed to normoxia or hyperoxia from the 3rd-14th day of life (n = 4 litters with 5-7 neonatal mice/litter per exposure group). FiO_2, fraction of inspired oxygen. SPF, specific-pathogen-free.
B) Representative photomicrographs of the distal lung sections of 14-day-old mice.
C) Hyperoxia exposure is associated with alterations in lung morphology and function. Data are shown as mean ± SEM, with significance testing by two-tailed *t*-test.
D) Volcano plot of ileal gene expression array showing gene expression altered by hyperoxia exposure.
E) Heatmap showing genes regulated by hyperoxia exposure.
F) Principal components analysis showing differential clustering of normoxia and hyperoxia exposed ileal genes. PC, principal component.
G) Ileal antimicrobial peptide expression is decreased in hyperoxia-exposure mice.
H) Community diversity of the adherent and luminal ileal bacterial microbiome is not significantly altered by hyperoxia exposure.
I) The relative abundance of an operational taxonomic units (OTU 002) that aligns to the genus *Staphylococcus* increases after hyperoxia exposure, as do OTUs aligning to *Corynebacterium* (OTU 124) and *Romboutsia* (OTU 013). Data are shown as mean ± SEM, with significance testing by two-tailed *t*-test.
J) Principal coordinates analysis of Bray-Curtis dissimilarity show global alterations in community composition in hyperoxia-exposed mice. Significance testing by permutational ANOVA (PERMANOVA), with equivocal dispersion confirmed by permutational multivariate analysis of dispersion (PERMDISP). PC, principal component.
K) Loading plot of principal components analysis of Hellinger transformed Euclidian distances showing the contribution of specific genera to the global community composition.
Schematic in (A) was generated using BioRender. See also Figures S1 and S2.

associated with alterations in the microbiota. Here, we asked if hyperoxia-induced alterations in intestinal AMP expression could alter the composition of the intestinal microbiota, creating a feedback loop that modulates inflammation in the developing lung.

RESULTS

Hyperoxia exposure alters lung morphology and function.

To examine potential mechanistic connections between the effects of supraphysiological oxygen exposure on the intestine and on the lungs, we utilized a well-established model of bronchopulmonary dysplasia[6,7] and exposed newborn mouse pups to hyperoxia (fraction of inspired oxygen, FiO_2, 0.85), and their littermate controls to normoxia (FiO_2 0.21), from the third to the 14th day of life (P3-P14, Fig. 1A). We reproduced well-described hyperoxia-induced alterations in lung structure and function (Fig. 1B-C)[8]. We also observed changes in the pulmonary transcriptome and related regulatory pathways (Fig. S1) that are consistent with similar observations[9–12] showing type 2 immune polarization and extensive alterations in alveolar epithelial, endothelial and fibroblast cell populations in response to hyperoxia-induced lung injury.

Intestinal antimicrobial peptide expression is altered in hyperoxia-exposed neonatal mice.

To interrogate potential hyperoxia-induced alterations in the neonatal gut, we then examined transcriptomic changes in the terminal ileum. Intriguingly, we found that hyperoxia-exposed mice had a significantly altered ileal transcriptome (Figure 1D-G). Global gene expression patterns were significantly altered (Figure 1D-F), including the prototypical AMP lysozyme (*Lyz1*, 4.2-fold decrease, FDR p = 0.012, Figure 1G, Table S1). In addition to other AMPs, additional markers of ileal Paneth cells were also decreased (*Pnliprp2*, 5.0-fold decrease; *Reg3g*, 2.7-fold decrease; and *Guca2b*, 2.4-fold decrease. Table S1). We verified these alterations in AMPs using qPCR (Figure S2A). Together, these results suggest that hyperoxia exposure reduces expression of intestinal AMPs.

The intestinal microbiota responds to pulmonary hyperoxia exposure.

We have reported that axenic (microbiota-free) mice devoid of a microbiome are protected[13], while

antibiotic-exposed mice with a disrupted microbiome are more susceptible, to hyperoxia-induced lung injury[7]. Together, these and other studies[14], suggest that the intestinal microbiota may modulate hyperoxia-induced lung injury. Because of this evidence, and due to our observation of changes in the transcription of potentially microbiota-altering AMPs, we asked if hyperoxia exposure altered the intestinal microbiota. To answer this question, we collected the intact terminal ileum from hyperoxia-exposed neonatal mice and littermate controls, which had been raised under specific pathogen-free (SPF) conditions and performed 16S rRNA MiSeq to define both the adherent and luminal ileal microbiome.

We found the global community composition but not diversity of the ileal microbiota was significantly altered by exposure to hyperoxia (p = 0.0014, pseudo-F = 6.3401, permutational ANOVA (PERMANOVA) of Bray-Curtis dissimilarity, p = 1, permutational multivariate analysis of dispersion (PERMDISP), Figure 1H-K). The first and second principal components are driven primarily by the abundance of the genus *Staphylococcus* and several uncultured *Ligilactobacillus* species (Figure 1J). In unadjusted univariate analysis, we identified increases in taxa aligning to the genera *Staphylococcus*, *Corynebacterium* and *Romboutsia* (Figure 1I). We verified these alterations using negative binomial regression (Figure S2), which also detected significant alterations in *Proteus* and Lachnospiraceae NK4A136 group. Correlation analysis between these differentially abundant genera and our validation qPCR for key AMPs supports a direct link between the expression of *Lyz1* and the relative abundance of *Staphylococcus* (Figure S2F). Together, these results suggest hyperoxia exposure alters the ileal microbiome by increasing the expression of lysozyme which is associated with an increase in the relative abundance of *Staphylococcus*.

Hyperoxia directly suppresses intestinal epithelial AMP expression.

We turned to small intestinal organoids to directly test the capacity for hyperoxia exposure to depress intestinal AMP expression. We exposed organoids to either hyperoxia (FiO_2 0.95) or normoxia (FiO_2 0.21) for 24 hours (Figure 2A). In general, live imaging with visual light microscopy and immunohistochemistry demonstrated organoids maintained similar shape and cellular composition in both normoxia and hyperoxia (Figure 2B-C, Figure S3), but with a decrease in epithelial integrity (p < 0.0001, two-tailed t-test, Figure 2B). RNAseq revealed transcriptomic changes that generally recapitulated the changes observed in hyperoxia-exposed mice (Figure 2D-G). Principal components analysis shows a clear separation in gene expression between hyperoxia and normoxia-exposed organoids (Figure 2D), which is also reflected in a heatmap of regulated genes (Figure 2E). Pathway analysis showed extensive upregulation of genes associated with cellular inflammatory response and response to injury (Figure 2G). Like *in vivo*, we also noted a decrease in several Paneth cell markers (Table S2). We verified the relative expression of several genes by qPCR. As indicated in our transcriptomic data, *Lyz1* was decreased in mice exposed to hyperoxia, as was the defensin *Defa2* and the Paneth cell marker *Pnliprp2* (Figure S2A). Together these data suggest that the downregulation of AMP expression is linked to cellular damage response of the ileal epithelium from exposure to supraphysiologic oxygen.

Augmentation of lysozyme improves lung function in hyperoxia-exposed mice.

Having shown that exposure to supraphysiologic oxygen resulted in depressed expression of intestinal AMPs and an altered microbiome, we next wanted to test if AMP expression drove this effect. Lysozyme is the principal AMP, and expression is reduced in early life on most mucosal surfaces[15]. To test if the suppression of AMP expression in hyperoxia-exposed mice might have functional consequences, we repeated the hyperoxia-exposure experiment above using nearly genetically identical mice (C57BL/6NCrl, Figure 3A). However, to naturally vary their microbiota as much as possible, we purchased these animals from a different vendor and raised them in a different SPF vivarium. We exposed a randomly selected subset of

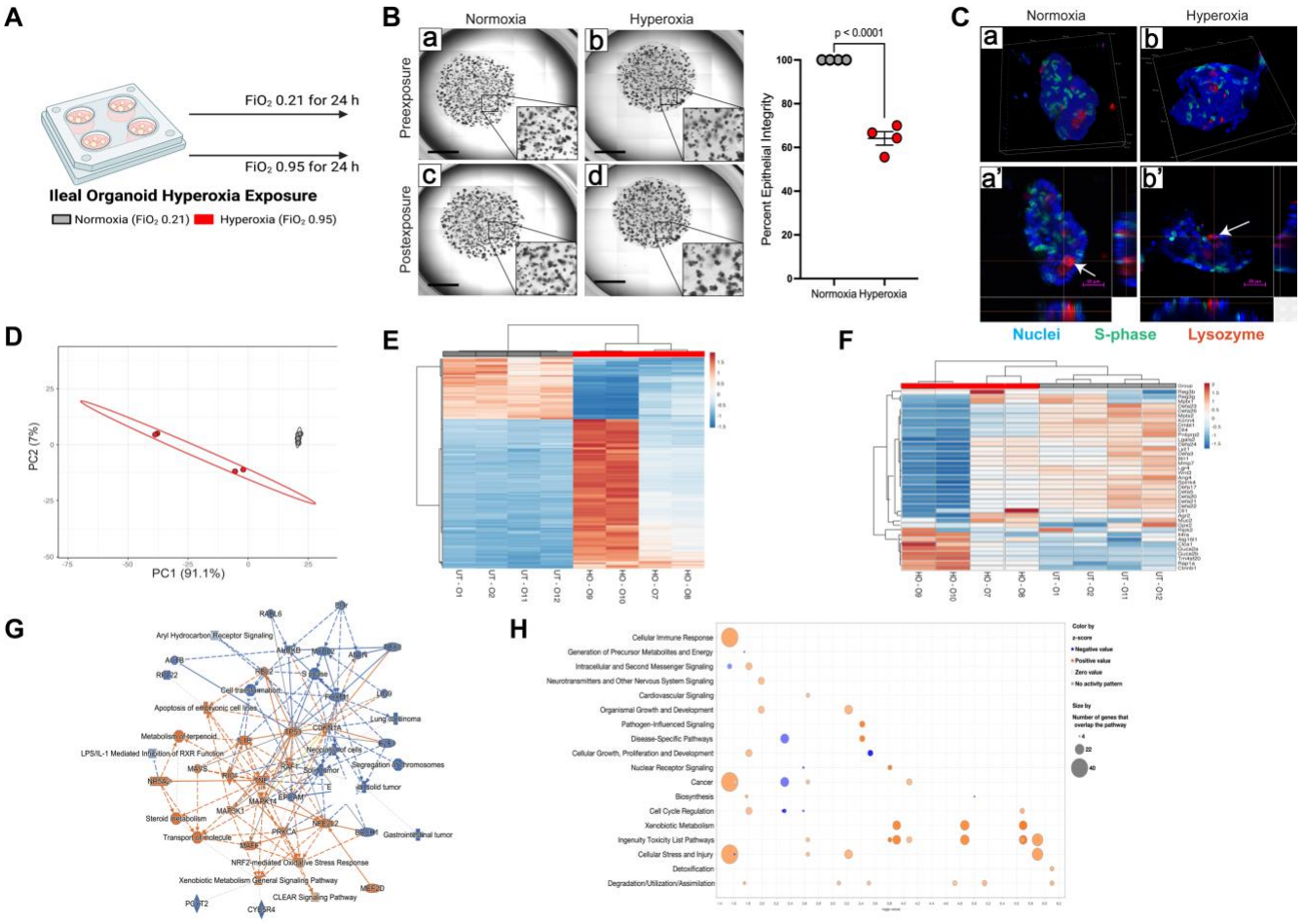

Figure 2. Antimicrobial peptide expression is reduced in hyperoxia-exposed intestinal organoids.

A) Small intestinal spheroid organoids derived from neonatal C57BL/6J mice were exposed to either hyperoxia or normoxia for 24 hours. FiO_2, fraction of inspired oxygen.

B) Representative images of organoids before and after exposure, with insets at 40x magnification. The percentage of organoids with healthy appearing epithelium declined in hyperoxia-exposed organoids. Data are shown as mean ± SEM, with significance testing by a two-tailed *t*-test. Scale bar represents 1000 μm.

C) Representative immunohistochemistry after exposure to normoxia or hyperoxia. Nuclei in blue, actively proliferating cells in green, and lysozyme-positive cells in red. Arrows identify lysozyme-positive Paneth cells. Scale bar represents 25 μm.

D) Principal components analysis showing differential clustering of normoxia and hyperoxia exposed ileal genes. PC, principal component.

E) Heatmap showing genes regulated by hyperoxia exposure.

F) Heatmap of antimicrobial peptide expression is decreased in hyperoxia-exposure organoids.

G) Ingenuity pathway analysis showing regulated pathways in hyperoxia or normoxia.

H) Bubble plot showing up and down-regulated pathways from hyperoxia exposure.

The schematic in (A) was generated using BioRender.

their neonates to lysozyme by oral gavage and compared them to unexposed littermates. Surprisingly, augmenting intestinal lysozyme improved lung structure and function after hyperoxia exposure (MLI $p < 0.0001$, RAC $p < 0.0001$, and resistance $p = 0.0212$, two-way ANOVA, Figure 3B-C).

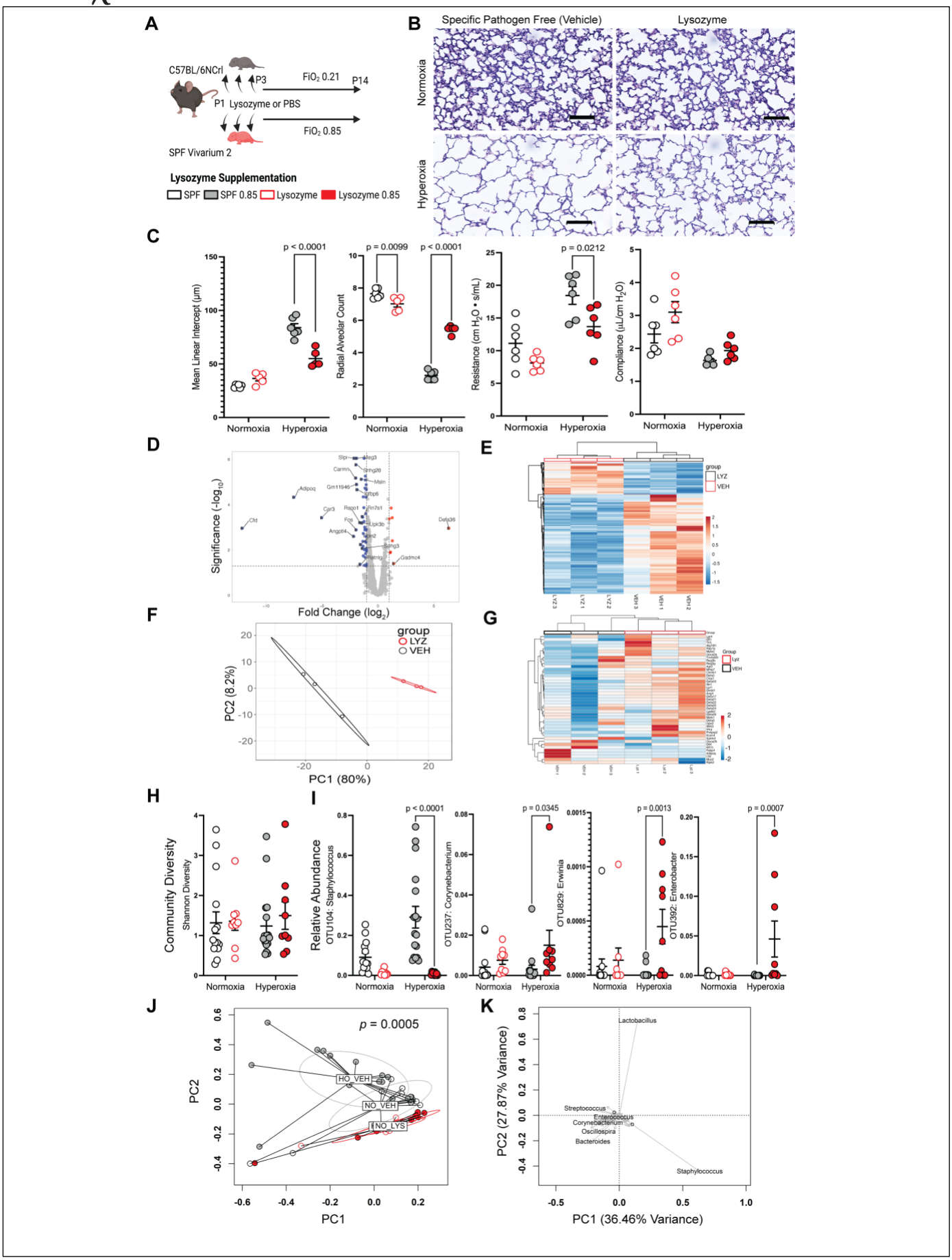
A
C57BL/6NCrl
P1
P3
P14
Lysozyme or PBS
FiO2 0.21
FiO2 0.85
SPF Vivarium 2
Lysozyme Supplementation
SPF
SPF 0.85
Lysozyme
Lysozyme 0.85
B
Specific Pathogen Free (Vehicle)
Lysozyme
Normoxia
Hyperoxia
C
p < 0.0001
p = 0.0099
p < 0.0001
p = 0.0212
Mean Linear Intercept (µm)
Radial Alveolar Count
Resistance (cm H2O • s/mL)
Compliance (µL/cm H2O)
Normoxia
Hyperoxia
D
Significance (-log10)
Fold Change (log2)
E
group
LYZ
VEH
F
group
LYZ
VEH
PC2 (8.2%)
PC1 (80%)
G
H
Community Diversity
Shannon Diversity
I
Relative Abundance
OTU104: Staphylococcus
OTU237: Corynebacterium
OTU829: Erwinia
OTU392: Enterobacter
p < 0.0001
p = 0.0345
p = 0.0013
p = 0.0007
J
p = 0.0005
HO_VEH
NO_VEH
NO_LYS
PC2
PC1
K
Lactobacillus
Streptococcus
Enterococcus
Corynebacterium
Oscillospira
Bacteroides
Staphylococcus
PC2 (27.87% Variance)
PC1 (36.46% Variance)

Figure 3 (Preceding Page). Intestinal lysozyme supplementation reduces hyperoxia-induced lung injury.
A) Neonatal C57BL/6NCrl mice randomized to either every other day exposure to lysozyme by gastric gavage or their littermate controls were then exposed to normoxia or hyperoxia from the 3rd-14th day of life (n = 4 litters with 5-7 neonatal mice/litter per exposure group). FiO_2, fraction of inspired oxygen. PBS, phosphate-buffered saline (vehicle). SPF, specific-pathogen-free.
B) Representative photomicrographs of the distal lung sections of 14-day-old mice.
C) Lysozyme exposure ameliorates hyperoxia-induced disruptions in lung morphology and function. Data are shown as mean ± SEM, with significance testing by two-way ANOVA.
D) Volcano plot of ileal RNAseq showing gene expression altered by lysozyme exposure.
E) Heatmap showing genes regulated by lysozyme exposure.
F) Principal components analysis showing differential clustering of ileal genes in lysozyme exposed mice. PC, principal component.
G) Ileal antimicrobial peptide expression is altered in lysozyme-exposed mice.
H) The community diversity of the adherent and luminal ileal bacterial microbiome is not significantly altered by lysozyme exposure.
I) The hyperoxia-induced increase in the relative abundance of operational taxonomic unit 014 (*Staphylococcus*) is ameliorated by lysozyme exposure. Multiple other genera are increased in lysozyme and hyperoxia-exposed mice. Data are shown as mean ± SEM, with significance testing by two-way ANOVA.
J) Principal coordinates analysis of Bray-Curtis dissimilarity show global alterations in community composition in lysozyme exposed mice. Significance testing by permutational ANOVA (PERMANOVA), with equivocal dispersion confirmed by permutational multivariate analysis of dispersion (PERMDISP). PC, principal component.
K) Loading plot of a principal components analysis of a Hellinger transformed Euclidian distance showing global community composition significantly altered in lysozyme-exposed mice.
The schematic in (A) was generated using BioRender. See also Figure S3.

Lysozyme augmentation increases intestinal AMP expression.

To identify alterations in intestinal AMP expression resulting from lysozyme exposure, we performed RNAseq using the terminal ileum of normoxia exposed mice. Intriguingly, we found that lysozyme-exposed mice had a significantly altered ileal transcriptome (Figure 3D-G). Global gene expression patterns were significantly altered (Figure 3D-F), including altered expression of multiple AMPs (Figure 3G). Of note, *Lyz1* expression increased 2.433-fold (FDR $p = 0.0004$). Together, these results suggest that dietary lysozyme exposure alters expression of the ileal transcriptome and results in additional ileal lysozyme production in an apparent feed-forward mechanism.

Lysozyme alters the intestinal microbiota.

We next asked if supplementary lysozyme altered the intestinal microbiota. Oral lysozyme supplementation produced a marked change in the overall composition of the ileal microbiota as compared to littermate controls ($p < 0.0001$, pseudo-$F = 0.2544$, PERMANOVA; $p = 0.7824$, PERMDISP, Figures 3J and S4), without significantly altering the community diversity (Figure 3H). On univariate analysis, multiple species were differentially abundant (Figure 3I). Most intriguing, the robust increase of *Staphylococcus* in hyperoxia-exposed Jackson Laboratory mice, was replicated in the vehicle and hyperoxia-exposed SPF Charles River mice but suppressed in lysozyme-exposed animals ($p < 0.0001$, two-way ANOVA, Figure 3I). Robust increases were also observed in mice exposed to both lysozyme and hyperoxia. *Corynebacterium*, *Erwinia,* and *Enterobacter* also increased in these doubly exposed mice ($p = 0.0345$, $p = 0.013$, $p = 0.0007$, two-way ANOVA, Figure 3H). MaAsLin 2 and binomial regression identified a shared 48 OTUs altered by lysozyme exposure (Figure S4) in addition to these four genera. Together, these analyses suggest that augmenting dietary lysozyme results in a robust alteration of the ileal microbiome and ameliorates the increase in *Staphylococcus* that otherwise occurs with hyperoxia exposure.

Lysozyme augmentation alters the pulmonary transcriptome.

We next sought to examine if the functional improvements we identified in the lungs of mice exposed to lysozyme were associated with differences in the lung transcriptome. Indeed, RNAseq revealed extensive alterations in gene expression in the lung (Figure 4). While the most increased inflammatory

related genes remained elevated in lysozyme and hyperoxia-exposed mice they were reduced as compared to controls exposed only to hyperoxia (Table S3). Similar patterns exist for genes related to endothelial regulation (Table S4). However, multiple genes exhibited opposite regulation in lysozyme-exposed mice (Table S5). Overall, the most reduced genes in hyperoxia exposure, were reduced regardless of lysozyme exposure (Figure 4A-B). The genes with the most increased expression were similar (Figure 4A-B). However, notable differences in *Hpgd*, *Akr1b8*, *Timp1* and *Zmat3* were appreciable. Altogether, 432 genes were differentially regulated in vehicle-exposed controls (Figure 4C) of which 271 were also differentially regulated the lysozyme exposed mice (Figure 4D), leaving 149 unique differentially regulated genes in lysozyme exposed mice (Figure 4E). The most significantly upregulated pathways in vehicle-exposed controls, included fibrosis, wound healing and IL-6-type cytokine signaling-related pathways (Figure 4F). However, different fibrosis-related and acute phase response pathways were upregulated in lysozyme-exposed mice (Figure 4F). Together, these transcriptional differences characterize a unique response to hyperoxia in the lungs of mice exposed to lysozyme, that is associated with ameliorated injury and an improvement in lung structure and function.

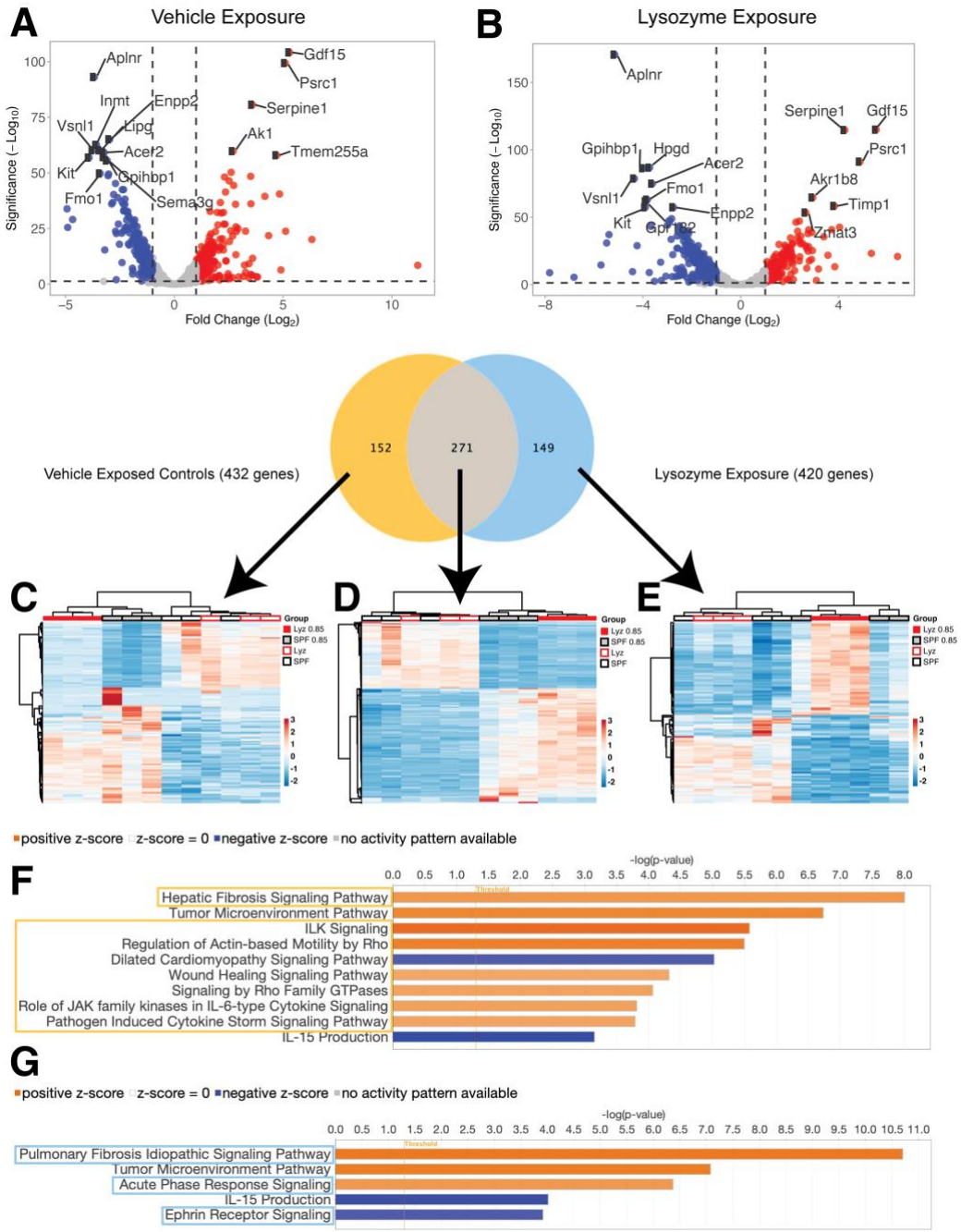

Figure 4 (Preceding Page). Lysozyme exposure alters the lung transcriptome.

A) Volcano plot showing hyperoxia alters gene expression in vehicle-exposed controls.

B) Volcano plot showing lysozyme exposure alters gene expression in the lung.

C) Heatmap showing differentially expressed genes in vehicle-exposed controls.

D) Heatmap showing similarly expressed genes between all groups.

E) Heatmap showing differentially expressed genes in lysozyme-exposed mice.

F) Major pathways altered in mice only exposed to normoxia or hyperoxia.

G) Major pathways altered in lysozyme-exposed mice.

DISCUSSION

Here, we have shown that exposure to supraphysiologic oxygen alters intestinal AMP expression, creating a microbiota-mediated response that modulates lung injury. Hyperoxia inhibited AMP transcription, both *in vivo* in neonatal mice and *in vitro* in intestinal organoids. *In vivo*, this altered the intestinal microbiota. Conversely, augmenting AMP expression altered the intestinal microbiota and improved lung injury. This reciprocal relationship between intestinal AMPs and lung injury demonstrates a gut-lung axis mechanism that can influence hyperoxia-exposure-induced lung injury. Together, these findings suggest intestinal AMPs are potential modulators of lung injury and repair.

AMPs are small cationic peptides that play a key role in host defense against microbes[16]. AMPs have broad antimicrobial activity and can kill or inhibit the growth of bacteria, fungi, and viruses[17]. AMPs, therefore, also play a key role in the regulation of the intestinal microbiota[16]. However, the potential bioactive effects of AMPs are not exclusively related to manipulating the microbiota. Lysozyme, the major AMP, can directly reduce the propagation of reactive oxygen species in colitis by releasing bacterial superoxide dismutase from *Lactobacillus lactis*[18]. Numerous species of bacteria within the microbiota contain superoxide dismutase genes[18]. This suggests potential mechanisms by which the redox balance of the intestinal epithelium might be influenced by alterations in AMP expression.

Multiple potential links between the lung and the gut have been proposed to explain the gut-lung axis[21]. Samuelson and colleagues[22] have proposed that microbes or microbial components may be trafficked to the lung via the lymph. Similarly, metabolites produced or modified by the intestinal microbiota, such as small-chain fatty acids, may also influence lung physiology[23]. Lysozyme can also liberate ligands for nucleotide binding oligomerization domain containing 1 (Nod1) from bacterial cell wall peptidoglycans. Circulating Nod1 ligands may reach the lung directly or may participate in immune cell maturation in the gut to determine the set points of the innate immune system in early life[24,25], and to educate the adaptive immune system[26]. The AMP-mediated gut-lung axis we describe here could impact some or all these potential pathways.

Exposure to supplemental oxygen is one of the most ubiquitous clinical interventions. Preterm infants, particularly the most immature, often require exposure for prolonged periods[2]. The disastrous effects of such exposure on the structure and function of neonatal lungs are well described[3]. In the adult gut, the gradient between hypoxia to anoxia across the radial axis of the gut has a profound influence on the composition of the intestinal microbiota and contributes to the maintenance of distinct communities of adherent and luminal microbes[27,28]. Hyperbaric oxygen exposure can shift the composition of these mature communities[27,28], as can inflammation, which alters the oxygen gradient in enterocytes[29]. However, the maturation of intestinal microbial communities is a developmental process, and initially, during the newborn period, the gut lumen is less hypoxic[30]. Recent evidence suggests that this process is driven by the accumulation of microbial biomass in the more distal intestine[30]. This is supported by the developmental progression from aerobic to facultative anaerobic microbes in the neonatal gut, and by the observation that while the intestinal lumen of axenic mice is anaerobic this appears to be driven by a slower chemical process[30]. This suggests our findings may be influenced by a unique developmental window created by the immature gut being more vulnerable to oxidative stress and the immature microbiota being less capable of functioning as an anoxic sink.

In adult mice, hyperoxia exposure has been shown to alter the lung and intestinal microbiota. Ashley and colleagues observed an increase in the oxygen-tolerant genera *Staphylococcus* after 72 hours of exposure to supraphysiological oxygen[14]. We observed a similar increase in *Staphylococcus* in the ileal microbiota of neonatal mice exposed to hyperoxia that replicated

robustly in mice with different starting microbiomes. While Ashley and colleagues confirmed a previously described[29] decrease in the Ruminococcaceae after hyperoxia exposure in the cecal microbiota of these adult mice[14], several differences likely explain our divergent findings. First, we sampled the ileal microbiota, which is more translationally relevant to neonatal intestinal pathology. Second, our neonatal mice were considerably smaller and exposed to hyperoxia for a longer duration, which would be intolerable for adult mice. Finally, their intestinal microbiota were in an earlier stage of community formation, which places their microbial communities under considerably different ecological pressures. Intriguingly, this increase in *Staphylococcus* was ameliorated in our lysozyme-exposed and associated with less severe lung injury. In subsequent experiments, Ashley and colleagues further found that adult axenic mice were protected from lung injury, and antibiotic-exposed mice experienced worse lung injury[14] - findings we have previously demonstrated in neonatal mice[7,13].

Under SPF conditions, the intestinal microbiota of co-housed mice converges over time[31,32], and the primary source of the intestinal microbiota is almost universally the mother but may show some littermate effects[33,34]. We took multiple steps to address these factors in these experiments. First, we intentionally varied the initial microbiota of the maternal mice as much as possible by purchasing them from two different animal vendors, cage-randomizing them for cohousing on arrival, and acclimatizing them in two different SPF vivaria before breeding. Second, to limit a littermate effect, we took the newborn mice from two simultaneously born litters and randomly redistributed them between their two mothers on the day of birth. We then assigned one pooled litter to hyperoxia and the other to normoxia and rotated the mothers daily to minimize their unique contributions. For exposure to lysozyme, we randomly selected newborn mice within these homogenized litters and used their unexposed littermates as controls. Because this approach likely underestimates the potential microbiota effects of lysozyme exposure due to littermate cross-contamination, it underscores that increase in *Staphylococcus* abundance with hyperoxia exposure is robust, since we replicated it across a wide range of initial microbiomes.

In summary, we have described a gut-lung axis driven by intestinal AMP expression and mediated by the intestinal microbiota that influences hyperoxia-induced lung injury. These murine and organoid experiments suggest that AMP expression represents a potential therapeutic target to modulate the intestinal microbiota and the response to lung injury. These results have implications for the clinical management of premature infants in neonatal care at high risk of developing bronchopulmonary dysplasia.

METHODS SUMMARY

Detailed methods are provided below and include the following:

- KEY RESOURCES TABLE
- RESOURCE AVAILABILITY
  - Lead contact
  - Materials availability
  - Data and code availability
- EXPERIMENTAL MODEL AND SUBJECT DETAILS
  - Animals
  - Mouse intestinal spheroid organoids
- METHOD DETAILS
  - FlexiVent pulmonary function
  - Histology and morphometry
  - Immunohistochemistry
  - Generation of intestinal organoids
  - Organoid hyperoxia experiment
  - Transcriptomics
  - Microbiome analysis
  - Bioinformatics
  - Statistical analysis

Acknowledgments:

Research reported in this article was supported by the NIH: K08 HL151907 (KW), K08 HL141652 (CL), K08 DK120871 (AO), 1U01ES027697 (TJ) and R21ES031559 (TJ); the Kaul Pediatric Research Institute at Children's of Alabama (KW); the Microbiome Center at UAB (KW); and the Harvard Digestive Disease Center (AO). The authors thank Joseph Pierre for his advice.

Author contributions:

Conceptualization: NA, AO, TJ, KW. Experimentation: AA, TN, BH, KT, CA, PJ, CR, AO, TJ, KW. Analysis: IM, NA, AO, TJ, KW. Supervision: AO, TJ, KW. Manuscript: KW. All authors approved of the final submitted version of the manuscript.

Declaration of Interests:

CL is the founder and CEO of Alveolus Bio and Resbiotic, Inc., NA and KW are advisors, and TN is now an employee.

Inclusion and Diversity:

We support the inclusive, diverse, and equitable conduct of research. We worked to ensure sex balance in the selection of non-human subjects. Multiple authors of this paper self-identify as an underrepresented ethnic minority in their field of research, as a gender minority, or as a member of the LGBTQA+ community. While citing references scientifically relevant to this work, we also actively worked to promote gender balance in our reference list.

REFERENCES

1. Nikolić, M.Z., Sun, D., and Rawlins, E.L. (2018). Human lung development: recent progress and new challenges. Development *145*, dev163485. 10.1242/dev.163485.
2. Hauspurg, A.K., Allred, E.N., Vanderveen, D.K., Chen, M., Bednarek, F.J., Cole, C., Ehrenkranz, R.A., Leviton, A., and Dammann, O. (2011). Blood Gases and Retinopathy of Prematurity: The ELGAN Study. Neonatology *99*, 104–111. 10.1159/000308454.
3. Thébaud, B., Goss, K.N., Laughon, M., Whitsett, J.A., Abman, S.H., Steinhorn, R.H., Aschner, J.L., Davis, P.G., McGrath-Morrow, S.A., Soll, R.F., et al. (2019). Bronchopulmonary dysplasia. Nat Rev Dis Primers 5, 78. 10.1038/s41572-019-0127-7.
4. Mookherjee, N., Anderson, M.A., Haagsman, H.P., and Davidson, D.J. (2020). Antimicrobial host defence peptides: functions and clinical potential. Nat Rev Drug Discov 19, 311–332. 10.1038/s41573-019-0058-8.
5. Lecaille, F., Lalmanach, G., and Andrault, P.-M. (2016). Antimicrobial proteins and peptides in human lung diseases: A friend and foe partnership with host proteases. Biochimie *122*, 151–168. 10.1016/j.biochi.2015.08.014.
6. Nardiello, C., Mižíková, I., Silva, D.M., Ruiz-Camp, J., Mayer, K., Vadász, I., Herold, S., Seeger, W., and Morty, R.E. (*2017*). Standardisation of oxygen exposure in the development of mouse models for bronchopulmonary dysplasia. Disease models & mechanisms 10, 185–196. 10.1242/dmm.027086.
7. Willis, K.A., Siefker, D.T., Aziz, M.M., White, C.T., Mussarat, N., Gomes, C.K., Bajwa, A., Pierre, J.F., Cormier, S.A., and Talati, A.J. (2019). Perinatal maternal antibiotic exposure augments lung injury in offspring in experimental bronchopulmonary dysplasia. American Journal of Physiology - Lung Cellular and Molecular Physiology 3, 21. 10.1152/ajplung.00561.2018.
8. Berger, J., and Bhandari, V. (2014). Animal models of bronchopulmonary dysplasia. The term mouse models. American Journal of Physiology - Lung Cellular and Molecular Physiology *307*, L936-47. 10.1152/ajplung.00159.2014.
9. Hurskainen, M., Mižíková, I., Cook, D.P., Andersson, N., Cyr-Depauw, C., Lesage, F., Helle, E., Renesme, L., Jankov, R.P., Heikinheimo, M., et al. (2021). Single cell transcriptomic analysis of murine lung development on hyperoxia-induced damage. Nat Commun 12, 1565. 10.1038/s41467-021-21865-2.
10. Mižíková, I., Lesage, F., Cyr-Depauw, C., Cook, D.P., Hurskainen, M., Hänninen, S.M., Vadivel, A., Bardin, P., Zhong, S., Carpén, O., et al. (2022). Single-Cell RNA Sequencing-Based Characterization of Resident Lung Mesenchymal Stromal Cells in Bronchopulmonary Dysplasia. Stem Cells *40*, 479–492. 10.1093/stmcls/sxab023.
11. Xia, S., Ellis, L.V., Winkley, K., Menden, H., Mabry, S.M., Venkatraman, A., Louiselle, D., Gibson, M., Grundberg, E., Chen, J., et al. (2022). Neonatal hyperoxia induces activated pulmonary cellular states and sex-dependent transcriptomic changes in a model of experimental bronchopulmonary dysplasia. Am J Physiol-lung C. 10.1152/ajplung.00252.2022.
12. Cantu, A., Gutierrez, M.C., Dong, X., Leek, C., Sajti, E., and Lingappan, K. (2022). Remarkable sex-specific differences at Single-Cell Resolution in Neonatal Hyperoxic Lung Injury. Am J Physiol-lung C. 10.1152/ajplung.00269.2022.
13. Dolma, K., Freeman, A.E., Rezonzew, G., Payne, G.A., Xu, X., Jilling, T., Blalock, J.E., Gaggar, A., Ambalavanan, N., and Lal, C.V. (2019). Effects of Hyperoxia on Alveolar and Pulmonary Vascular Development in Germ Free Mice. American Journal of Physiology - Lung Cellular and Molecular Physiology *295*, L86. 10.1152/ajplung.00316.2019.
14. Ashley, S.L., Sjoding, M.W., Popova, A.P., Cui, T.X., Hoostal, M.J., Schmidt, T.M., Branton, W.R., Dieterle, M.G., Falkowski, N.R., Baker, J.M., et al. (2020). Lung and gut microbiota are altered by hyperoxia and contribute to oxygen-induced lung injury in mice. Science translational medicine 12, eaau9959. 10.1126/scitranslmed.aau9959.
15. Lokken-Toyli, K.L., Piters, W.A.A. de S., Zangari, T., Martel, R., Kuipers, K., Shopsin, B., Loomis, C., Bogaert, D., and Weiser, J.N. (2021). Decreased production of epithelial-derived antimicrobial molecules at mucosal barriers during early life. Mucosal Immunol 14, 1358–1368. 10.1038/s41385-021-00438-y.
16. Gong, T., Fu, J., Shi, L., Chen, X., and Zong, X. (2021). Antimicrobial Peptides in Gut Health: A Review. Frontiers Nutrition 8, 751010. 10.3389/fnut.2021.751010.
17. Luo, Y., and Song, Y. (2021). Mechanism of Antimicrobial Peptides: Antimicrobial, Anti-Inflammatory and Antibiofilm Activities. Int J Mol Sci 22, 11401. 10.3390/ijms222111401.
18. Ballal, S.A., Veiga, P., Fenn, K., Michaud, M., Kim, J.H., Gallini, C.A., Glickman, J.N., Quéré, G., Garault, P., Béal, C., et al. (2015). Host lysozyme-mediated lysis of Lactococcus lactis facilitates delivery of colitis-attenuating superoxide dismutase to inflamed colons. Proc National Acad Sci 112, 7803–7808. 10.1073/pnas.1501897112.
19. Geitani, R., Moubareck, C.A., Xu, Z., Sarkis, D.K., and Touqui, L. (2020). Expression and Roles of Antimicrobial Peptides in Innate Defense of Airway Mucosa: Potential Implication in Cystic Fibrosis. Front Immunol 11, 1198. 10.3389/fimmu.2020.01198.
20. Persson, L.J.P., Aanerud, M., Hardie, J.A., Nilsen, R.M., Bakke, P.S., Eagan, T.M., and Hiemstra, P.S. (2017). Antimicrobial peptide levels are linked to airway inflammation, bacterial colonisation and exacerbations in chronic obstructive pulmonary disease. Eur Respir J 49, 1601328. 10.1183/13993003.01328-2016.
21. Bingula, R., Filaire, M., Radosevic-Robin, N., Bey, M., Berthon, J.-Y., Bernalier-Donadille, A., Vasson, M.-P., and Filaire, E. (2017). Desired Turbulence? Gut-Lung Axis, Immunity, and Lung Cancer. Journal of oncology 2017, 5035371–15. 10.1155/2017/5035371.

22. Samuelson, D.R., Welsh, D.A., and Shellito, J.E. (2015). Regulation of lung immunity and host defense by the intestinal microbiota. Frontiers in microbiology 6, 1085. 10.3389/fmicb.2015.01085.
23. Singh, N., Gurav, A., Sivaprakasam, S., Brady, E., Padia, R., Shi, H., Thangaraju, M., Prasad, P.D., Manicassamy, S., Munn, D.H., et al. (2014). Activation of Gpr109a, Receptor for Niacin and the Commensal Metabolite Butyrate, Suppresses Colonic Inflammation and Carcinogenesis. Immunity 40, 128–139. 10.1016/j.immuni.2013.12.007.
24. Stevens, J., Steinmeyer, S., Bonfield, M., Peterson, L., Wang, T., Gray, J., Lewkowich, I., Xu, Y., Du, Y., Guo, M., et al. (2022). The balance between protective and pathogenic immune responses to pneumonia in the neonatal lung is enforced by gut microbiota. Sci Transl Med 14. 10.1126/scitranslmed.abl3981.
25. Gray, J., Oehrle, K., Worthen, G., Alenghat, T., Whitsett, J., and Deshmukh, H. (2017). Intestinal commensal bacteria mediate lung mucosal immunity and promote resistance of newborn mice to infection. Science translational medicine 9, eaaf9412. 10.1126/scitranslmed.aaf9412.
26. Macpherson, A.J., and Uhr, T. (2004). Induction of Protective IgA by Intestinal Dendritic Cells Carrying Commensal Bacteria. Science *303*, 1662–1665. 10.1126/science.1091334.
27. Gonzalez, C.G., Mills, R.H., Kordahi, M.C., Carrillo-Terrazas, M., Secaira-Morocho, H., Widjaja, C.E., Tsai, M.S., Mittal, Y., Yee, B.A., Vargas, F., et al. (2022). The Host-Microbiome Response to Hyperbaric Oxygen Therapy in Ulcerative Colitis Patients. Cell Mol Gastroenterology Hepatology 14, 35–53. 10.1016/j.jcmgh.2022.03.008.
28. Albenberg, L., Esipova, T.V., Judge, C.P., Bittinger, K., Chen, J., Laughlin, A., Grunberg, S., Baldassano, R.N., Lewis, J.D., Li, H., et al. (2014). Correlation Between Intraluminal Oxygen Gradient and Radial Partitioning of Intestinal Microbiota. Gastroenterology *147*, *105*5-1063.e8. 10.1053/j.gastro.2014.07.020.
29. Rivera-Chávez, F., Lopez, C.A., and Bäumler, A.J. (2017). Oxygen as a driver of gut dysbiosis. Free Radical Bio Med 105, 93–101. 10.1016/j.freeradbiomed.2016.09.022.
30. Friedman, E.S., Bittinger, K., Esipova, T.V., Hou, L., Chau, L., Jiang, J., Mesaros, C., Lund, P.J., Liang, X., FitzGerald, G.A., et al. (2018). Microbes vs. chemistry in the origin of the anaerobic gut lumen. Proc National Acad Sci 115, 4170–4175. 10.1073/pnas.1718635115.
31. Dickson, R.P., Erb-Downward, J.R., Falkowski, N.R., Hunter, E.M., Ashley, S.L., and Huffnagle, G.B. (2018). The Lung Microbiota of Healthy Mice are Highly Variable, Cluster by Environment, and Reflect Variation in Baseline Lung Innate Immunity. American Journal of Respiratory and Critical Care Medicine, rccm.201711-2180OC. 10.1164/rccm.201711-2180oc.
32. Mims, T.S., Abdallah, Q.A., Stewart, J.D., Watts, S.P., White, C.T., Rousselle, T.V., Gosain, A., Bajwa, A., Han, J.C., Willis, K.A., et al. (2021). The gut mycobiome of healthy mice is shaped by the environment and correlates with metabolic outcomes in response to diet. Commun Biology 4, 281. 10.1038/s42003-021-01820-z.
33. Robertson, S.J., Lemire, P., Maughan, H., Goethel, A., Turpin, W., Bedrani, L., Guttman, D.S., Croitoru, K., Girardin, S.E., and Philpott, D.J. (2019). Comparison of Co-housing and Littermate Methods for Microbiota Standardization in Mouse Models. Cell reports 27, 1910-1919.e2. 10.1016/j.celrep.2019.04.023.
34. Ringel-Scaia, V.M., Qin, Y., Thomas, C.A., Huie, K.E., McDaniel, D.K., Eden, K., Wade, P.A., and Allen, I.C. (2019). Maternal Influence and Murine Housing Confound Impact of NLRP1 Inflammasome on Microbiome Composition. J Innate Immun 11, 416–431. 10.1159/000495850.
35. Huang, Y.J., Erb-Downward, J.R., Dickson, R.P., Curtis, J.L., Huffnagle, G.B., and Han, M.K. (2017). Understanding the role of the microbiome in chronic obstructive pulmonary disease: principles, challenges, and future directions. Transl Res *179*, 71–83. 10.1016/j.trsl.2016.06.007.
36. Chotirmall, S.H., Bogaert, D., Chalmers, J.D., Cox, M.J., Hansbro, P.M., Huang, Y.J., Molyneaux, P.L., O'Dwyer, D.N., Pragman, A.A., Rogers, G.B., et al. (2022). Therapeutic Targeting of the Respiratory Microbiome. Am J Resp Crit Care. 10.1164/rccm.202112-2704pp.
37. Willis, K.A., Purvis, J.H., Myers, E.D., Aziz, M.M., Karabayir, I., Gomes, C.K., Peters, B.M., Akbilgic, O., Talati, A.J., and Pierre, J.F. (2019). Fungi form interkingdom microbial communities in the primordial human gut that develop with gestational age. FASEB journal : official publication of the Federation of American Societies for Experimental Biology 33, 12825–12837. 10.1096/fj.201901436rr.

PREPRINT

bioRχiv

Antimicrobial peptides modulate lung injury by altering the intestinal microbiota

Graphical Abstract

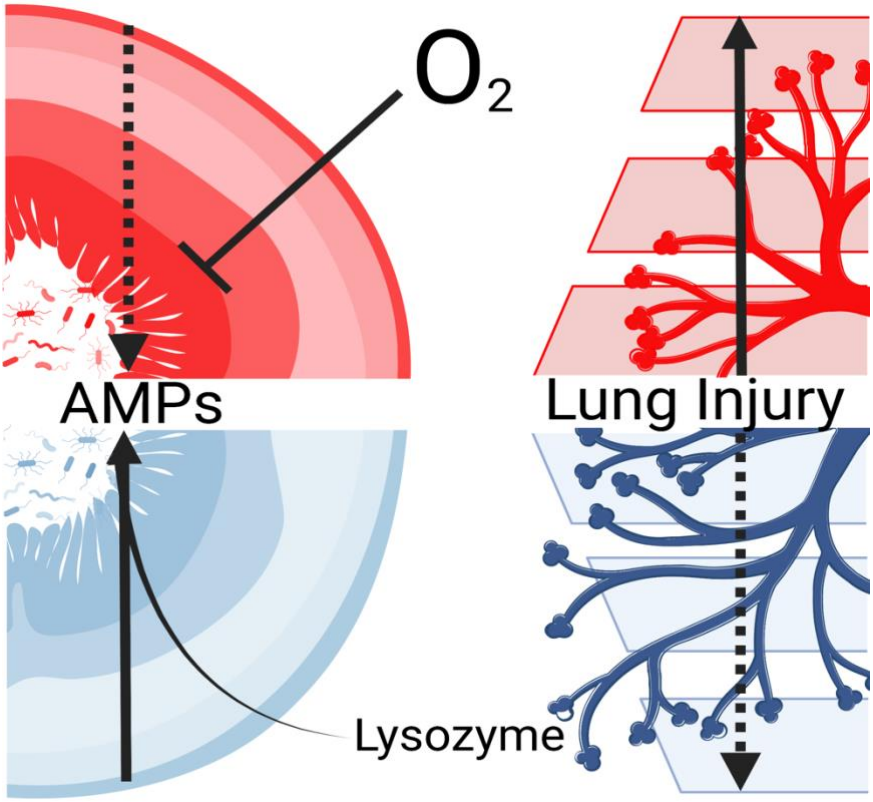

Authors

Ahmed Abdelgawad, Teodora Nicola, Isaac Martin … Amy E. O'Connell, Tamás Jilling, and Kent A. Willis

Correspondence

kawillis@uab.edu

In Brief

Using a combination of murine models and organoids, Abdelgawad and Nicola et al. find that suppression of antimicrobial peptide release by the neonatal intestine in response to supra-physiological oxygen influences the progression of lung injury likely via modulation of the ileal microbiota.

Highlights

- Supraphysiologic oxygen exposure alters intestinal antimicrobial peptides (AMPs).
- Intestinal AMP expression has an inverse relationship with the severity of lung injury.
- AMP-driven alterations in the intestinal microbiota form a gut-lung axis that modulates lung injury.
- AMPs may mediate a gut-lung axis that modulates lung injury.

METHOD DETAILS

Key Resource Table

Reagent	Company - Catalog #	RRID
Teklad S-2335 Mouse Breeder Sterilizable Diet	Envigo - 7904.15	
Lysozyme	Sigma Aldrich 12671-19-1	
zymoBIOMICS microbial community standards	Zymo Research - D6300 and D6310	
zymoBIOMICS microbial community DNA standards	Zymo Research - D6305/6306 and D6311	
zymoBIOMICS spike-in control I	Zymo Research - D6320-10	
zymoBIOMICS spike-in control II	Zymo Research - D6321-10	
zymoBIOMICS gut microbiome standard	Zymo Research - D6331	
RNase-free DNase Set	Qiagen - 79254	
QIAshredder	Qiagen - 79656	
PrimeScript RT Master Mix	Takara Biosciences - RR036B	
MouseWG-6 2.0	Illumina	
Bioanalyzer High Sensitivity DNA Analysis Kit	Agilent Technologies - 5067-4626	
Tissue Protein Extraction Reagent	Pierce Biotechnology - 78510	
Roche Complete Protease Inhibitor	Millipore Sigma - 11836153001	
Bradford Protein Assay Kit I	Bio-Rad - 5000001	
Protein Assay Standard I	Bio-Rad - 5000005	
Immun-Star™ WesternC™ Chemiluminescence Kit	Bio-Rad - 170-5070	
Paraformaldehyde, 4% w/v aq. soln.	TFS - 047392.9M	
Antigen Retrieval Buffer	Abcam - ab93678	
ProLong Diamond Anti-Fade Mounting Media with DAPI	TFS - P36962	RRID:AB_2307445
Click-iT EdU Cell Proliferation Kit for Imaging, AF 488 dye	TFS- C10337	
Small Intestine Organoid Media		

R Spondin-1 Conditioned Media (10mL)	HDDC Organoid Core	
Advanced DMEM/F-12 (85mL)	Life Technologies - 12634028	
Glutamax (100X) (1mL)	Life Technologies - 35050061	
HEPES (1M)(1mL)	Life Technologies - 15630080	
Primocin (50mg/mL) (200µL)	Invivogen - ant-pm-1	
Normocin (50mg/mL) (200µL)	Invivogen - ant-nr-1	
B27 Supplement (50X) (1mL)	Life Technologies 12587010	
N_2 Supplement (100X) (500µL)	Life Technologies 17502001	
N-Acetyl-Cysteine (500mM) (250µL)	Sigma - A7250	
Noggin (100ug/mL) (100µL)	Peprotech - 250-38	
EGF(500ug/mL) (10µL)	Peprotech - 315-09	
Antibodies		
Ghost Dye Violet 510	TonboBio - 13-0870-T100	
Mouse BD Fc Block (CD16/32)	BD Biosciences - 553142	RRID:AB_394656
Recombinant Anti-Lysozyme	Abcam - Ab108508	RRID:AB_10861277
Chromogranin A Polyclonal Antibody	TFS - PA5-77917	RRID:AB_2735659
Goat anti-Rabbit IgG Secondary Antibody, AF 555	Invitrogen - A-21428	RRID:AB_2535849
Goat anti-rabbit secondary antibody	Cell Signaling - 7074	RRID:AB_2099233
Donkey anti-goat secondary antibody	SouthernBiotech - 6402	RRID:AB_2796335
Goat anti-Rat IgG - Alexa Fluor™ 555	Invitrogen - A-21434	RRID:AB_2535855
Chicken anti-Mouse IgG - AF™ 647	Invitrogen- A-21463	RRID:AB_2535869
Goat anti-Rabbit IgG - AF™ 555	Invitrogen- A-21428	RRID:AB_2535849
Goat anti-Hamster IgG (H+L) Cross-Adsorbed Secondary Antibody, Alexa Fluor™ 647	Invitrogen - A-21451	RRID:AB_2535868
Primer Sequences		
Bacterial 16S, V4-V5, 450 bp	515F	GTGCCAGCGCCGCGGTAA
	907R	CCGTCAATTCCTTTGAGTTT
TaqMan Gene Expression Assay: *Lyz1*	Invitrogen - 4331182	Mm00657323_m1
Defa20, Defa2, Gm21002	Invitrogen - 4331182	Mm00842045_91

Pnliprp2	Invitrogen - 4331182	Mm00448214_m1
Dmbt1	Invitrogen - 4331182	Mm00455996_m1
Organisms		
C57Bl/6J mouse	Jackson Laboratory - 000664	RRID:IMSR_JAX:000664
C57BL/6NCrl mouse	Charles River - 027	RRID:IMSR_CRL:027
Equipment		
ProOx 360 controller	BioSpherix	RRID:SCR_021130
A1R HD confocal microscope	Nikon	RRID:SCR_020317
flexiVent	SCIREQ	RRID:SCR_022673
2100 Bioanalyzer Instrument	Agilent	RRID:SCR_018043
QuantStudio 6	Applied Biosciences	RRID:SCR_020239
Rotor-Gene Q Series	Qiagen	RRID:SCR_018976
NovoSeq 6000 system	Illumina	RRID:SCR_016387
MiSeq platform	Illumina	RRID:SCR_020133
HiSeq 4000 platform	Illumina	RRID:SCR_016386
Software		
FACSDiva	BD Biosciences - v9.0	RRID:SCR_001456
FlowJo for Mac	BD Biosciences - v10.8.1	RRID:SCR_008520
Rotor-Gene Q Series Software	Qiagen	RRID:SCR_015740
FIJI	https://fiji.sc	RRID:SCR_002285
Prism 9 for Mac	GraphPad - v9.4.1	RRID:SCR_002798
R	R project for statistical computing - v4.2.2	RRID:SCR_001905
RStudio	Posit - v2022.12.0+353	RRID:SCR_000432
Vegan, R Package	https://github.com/vegandevs/vegan - v2.6-4	RRID:SCR_011950
phyloseq, R Package	https://github.com/joey711/phyloseq - v1.42.0	RRID:SCR_013080
DESeq2, R Package	10.18129/B9.bioc.DESeq2 - v1.38.2	RRID:SCR_015687
MaAsLin2, R Package	https://github.com/biobakery/M	RRID:SCR_023241

	aaslin2 - v1.12.0	
tidyverse, R Package	https://www.tidyverse.org/ - v1.3.2	RRID:SCR_019186
caret, R Package	https://github.com/topepo/caret/ - v6.0-93	RRID:SCR_021138
SpiecEasi, R Package	https://github.com/zdk123/SpiecEasi - v1.1.2	RRID:SCR_022712
QIIME 2	QIIME 2 Core 2022.11	RRID:SCR_008249
SILVA	SILVA v138.1	RRID:SCR_006423
CLC Genomic Workbench	Qiagen - v22	RRID:SCR_011853
ClustVis	https://biit.cs.ut.ee/clustvis/	RRID:SCR_017133
Ingenuity Pathway Analysis	Qiagen (July 2022 edition)	RRID:SCR_008653
Datasets		
Gene-expression array, mouse	This paper	NCBI SRA: PRJNA931604
RNAseq, mouse	This paper	NCBI SRA: PRJNA931604
RNAseq, mouse organoid	This paper	NCBI SRA: PRJNA931604
16S rRNA MiSeq, mouse	This paper	NCBI SRA: PRJNA931604

Resource Availability

Lead Contact: Further information and requests for resources and reagents should be directed to and will be fulfilled by the lead contact, Dr. Kent Willis (kawillis@uab.edu).

Materials Availability: This study did not generate any unique reagents or transgenic animals.

Data Availability:

- 16S and RNA sequencing data were deposited at the NCBI Sequence Read Archive (BioProject ID: PRJNA931604).
- Gene expression array data were deposited at the NCBI Gene Expression Omnibus (Accession number: GSE125489).
- Processed data files are available at github.com/WillisLungLab/AMP.
- This manuscript does not report original code.
- All other data needed to evaluate the conclusions in the manuscript are available within the main text or supplementary materials.

Experimental Model Details

Animals:
Animal experimentation was performed at the University of Alabama at Birmingham. To broaden the translatability and reproducibility of the resulting experiments, we intentionally selected two similar, but not identical, mouse strains that we purchased from different animal vendors and raised in different vivaria to vary their initial microbiomes. In the first experiment, we used 8-week-old female C57Bl/6J mice (Stock Number 000664) purchased from the Jackson Laboratory (hence, JAX) and allowed to acclimate in specific-pathogen free (SPF) housing with 4 animals per cage, on a 12-hour light/dark cycle, at 20-24C, with *ad libitum* access to irradiated rodent chow (Teklad 7904, Envigo) in SPF Vivarium 1 (Pittman Biomedical Research Building II) for two weeks. Similarly, for the second experiment, we purchased C57Bl/6NCrl mice (Stock Number 027) from the Charles River Laboratory and acclimated them in SPF Vivarium 2 (Volker Hall) with the same diet for two weeks. Animal studies were performed in accordance with the recommendations in the Guide for the Care and Use of Laboratory Animals of the National Institutes of Health, under protocol 22042 approved by the Institutional Animal Care and Use Committee at UAB. Animal experimentation is reported in accordance with the ARRIVE guidelines[1]. We utilized our established, standardized hyperoxia-exposure model of BPD[2,3]. We time-mated the mice to produce multiple simultaneous birth cohorts with the same perinatal exposure. On the day of birth, pups from two consecutively born litters with the same perinatal exposure were pooled and the pups were re-distributed evenly between the two dams. Litter sizes for all experiments were adjusted to 5–8 pups per treatment group to minimize nutritional effects on lung development. One pooled litter was randomly assigned to hyperoxia [fraction of inspired oxygen (FiO_2) 0.85]) and the other to air (FiO_2 0.21). Pups were exposed continuously for 11 days, starting on the third day after birth until the 14th day (P3-14). Oxygen concentrations were maintained using a ProOx monitor (Biospherix). Dams were rotated daily between the two pooled litters to limit maternal complications of hyperoxia. Growth was monitored daily for all pups throughout the experiment.
For the lysozyme exposure experiment, pups from two pooled litters at time were randomized on P2 to either lysozyme exposure or vehicle exposure. Lysozyme exposure was performed via every other day

oral gavage of 10,000 units/gram in PBS to pups marked by tail clipping. Unmarked littermates were used as vehicle (PBS)-exposed controls. Experiments were repeated at least three times.

Mouse intestinal epithelial spheroid organoids:
Organoid modeling was performed at the Harvard Digestive Disease Center (HDDC) Organoid Core at Boston Children's Hospital. Crypts were collected from C57Bl6J mice and cultured in 50mL Matrigel and fed with 500mL murine enteroid media in a 24 well plate in a 37°C humidified incubator with 5% CO_2. Media was changed every 2-3 days for the duration of the cultures. Organoids were passaged every 7-10 days by dissolving the Matrigel in Cell Recovery Media with mechanical disruption.

Further Method Details

Forced oscillometry:
A subset of P14 mice not used for morphometry or transcriptomics were sedated with ketamine and xylazine via I.P. injection, and the flexiVent system (SCIREQ) was used to assess respiratory resistance and compliance as described(15, 17). Briefly, the mice were tracheotomized with the appropriately sized cannula secured with a silk ligature. The flexiVent then executed the neonatal mouse pulmonary function program using room air in the sedated, closed-chest animal. Calibration of the flexiVent was done using the tracheal cannula before each experiment. Lung volumes were measured by volume displacement after completion of the flexiVent measurements.

Histology and morphometry:
The right lung was gravity inflated to 20 cmH_2O via tracheal insertion of an angiocath with 4% formalin as described(7). Three random 4-5 µm sections from each lung were stained with hematoxylin and eosin. To perform morphometry, lung sections were digitized under x20 magnification and analyzed independently by two researchers blinded to the group assignments using established methods (7, 18–20). Alveolarization was quantified using the mean linear intercept (L_m) and radial alveolar counts (RAC).

Immunohistochemistry:
Organoids were kept in 1.5 ml Eppendorf tubes. Three tubes per group were fixed by 0.4% PFA. Samples were resuspended using a Wide Bore Pipet Tips in a blocking buffer (1% BSA, 1% normal donkey serum, 1% CD16/32 in PBS) for 30 min in RT, and then incubated for one hour with primary antibodies at RT in incubation buffer (1% BSA, 1% normal donkey serum, 0.3% Triton X-100, and 0.01% sodium azide in PBS). The samples then were washed in PBS, and then incubated for one hour with the corresponding secondary antibodies at RT in the incubation buffer. Samples were centrifuged and resuspended in the proper buffer for each step. Finally, samples were counterstained with Click-iT™ EdU Cell Proliferation Kit for Imaging, Alexa Fluor™ 488. Images were then captured using an A1R HD inverted confocal microscope.

Generation of intestinal organoids:
Organoids were generated from C57Bl/6 mice after euthanasia using CO_2 followed by cervical dislocation. Proximal duodenal tissue was dissected, and feculent matter was cleared using cold intraluminal PBS. The tissue was cut longitudinally and then cut into 0.5 cm pieces and cleaned repeatedly in PBS until the supernatant was cleared. The tissue was then placed in 2mM EDTA and incubated on ice with rocking for 30 minutes. The tissue was then shaken vigorously for 2 minutes to release crypts and pipetted up and down 25 times with a 10mL serological pipet while mixing simultaneously. The solution was passed through a 70uM filter, and the filtrate was collected into a new 50mL conical tube. The filtrate was centrifuged (5min at 300xg) and supernatant discarded. Dissociated cells were then washed three times in Advanced DMEM/F12, centrifuged (5min at 300xg) after each wash, and reconstituted in Matrigel (50uL/well) and plated in 24-well plates and incubated for 10 minutes

at 37 C. Next, 0.5mL growth media was added to the wells. Enteroids were fed with growth media every 2-3 days and passaged approximately every 7 days.

Murine Small Intestine (ENR) Media (100mL)

Component	Volume	Catalog #	Final Concentration	Purpose
Rspondin-1 Conditioned Media	10mL	HDDC Organoid Core	10%	Contributes Rspondin-1 for stem cell proliferation
Advanced DMEM/F-12	85mL	Life Technologies 12634028	85%	Contributes glucose, NEAAs, sodium pyruvate, phenol red
Glutamax (100X)	1mL	Life Technologies 35050061	1X	Contributes L-glutamine to support growth
HEPES (1M)	1mL	Life Technologies 15630080	10mM	pH buffer for CO2 changes
Primocin (50mg/mL)	200uL	Invivogen ant-pm-1	100ug/mL	Antibiotic
Normocin (50mg/mL)	200uL	Invivogen ant-nr-1	100ug/mL	Antibiotic
B27 Supplement (50X)	1mL	Life Technologies 12587010	0.5X	Growth supplement
N2 Supplement (100X)	500uL	Life Technologies 17502001	0.5X	Growth supplement
N-Acetyl-Cysteine (500mM)	250uL	Sigma A7250	1.25mM	Antioxidant
Noggin (100ug/mL)	100uL	Peprotech 250-38	100ng/mL	BMP inhibitor
EGF(500ug/mL)	10uL	Peprotech 315-09	50ng/mL	Epidermal growth factor, stimulates mitosis

Organoid hyperoxia experiment:

Organoid hyperoxia experiment. Intestinal organoids were generated as above and incubated in a hyperoxia chamber (StemCell Technologies) at 95% oxygen for 24 hours. After the hyperoxia was completed, the supernatant was removed and the organoids and Matrigel were collected in 0.5mL cell recovery media (Corning) per well and placed on ice for 40 minutes. The solution was then centrifuged (5 minutes at 300 g at 4C) and the supernatant was removed. The organoids were then either placed in 2% β-mercaptoethanol in RLT buffer or 4% paraformaldehyde for RNA isolation or fixation, respectively.

Transcriptomics:

25 mg tissue sections from either the left lower lobe of the lung or from the terminal ileum were bead-lysed in RLT buffer (Qiagen) supplemented with 1% (w/w) 2-mercaptoethanol and frozen. RNA was isolated from cells with RNeasy kit with Qiashredder cell disruption (Qiagen) and RNase-free DNase Set (Qiagen) on-column DNA digestion. DNA purity and concentration were assessed using an Agilent 2100 Bioanalyzer RNA Analysis chip (Eukaryote Total RNA Pico Series II) (Agilent Technologies). Samples from Exp. 1 underwent transcriptomic analysis using array-based gene expression analysis and samples from Exp. 2 using RNAseq.

For array-based gene expression analysis: Analysis of gene expression was performed using the MouseWG-6 v2.0 array (Illumina), following quality testing of mRNA using an Agilent 2100 Bioanalyzer. Data were analyzed in GeneSpring GX using two-way ANOVA and the multiple testing correction method of Benjamini–Hochberg. A fold change cutoff of ≥ ±2 was used to generate downstream data sets.

For RNAseq: Preparation of RNA library (mRNAlibrary preparation (poly A enrichment) and transcriptome sequencing (NovaSeq PE150 (6 G raw data per sample) was conducted by Novogene Co., LTD, using the HiSeq 2500 platform (Illumina) with a pair-end 150-nucleotide read length as described[4]. Raw sequencing data was mapped to the genome, raw and normalized counts (TPM) were determined, and differential gene expression was calculated using the CLC Genomic Workbench (Qiagen). Genes with adjusted p-value (q) < 0.05 and log(FoldChange) > 0.301 were considered as differentially expressed. Heatmaps and PC analyses/plots were generated using *ClustVis* [5]. Differentially expressed genes were used as input for Ingenuity IPA (Qiagen) to identify significantly regulated networks and pathways.

Microbiome analysis: A 1 cm section of liquid nitrogen snap-frozen terminal ileum was used to quantify the mouse intestinal microbiome because of the advantages in quantifying the adherent mucosal microbiota[6]. We used ZymoBIOMICS whole organism and DNA microbial community standards (Zymo Research) as well as sterile-filtered PBS to create pairs of positive and negative controls appropriate for each step of the sample collection and isolation procedure. Microbial DNA was extracted and sequenced using the MiSeq platform (Illumina) at the UAB Microbiome Core using 16S V3-4 (bacterial) using primers 515F-806R.

Bioinformatics: We used QIIME 2.0 to merge, cluster, and quality control 16S rRNA gene amplicon sequences. Operational taxonomic units (OTUs) were called based on the SILVA database using closed reference-based OTU clustering with PyNAST and taxonomy via UCLUST. OTU tables were exported into R where they were normalized, transformed and analyzed with the following packages: *vegan*, *tidyverse, phyloseq*, *DESeq2, Maaslin2*, *SpiecEasi,* and *caret*. Two samples were excluded for insufficient read depth (below 1000 OTUs). OTUs present in <10% of samples were removed, and the remaining OTUs were transformed by total sum scaling. Alpha diversity using the raw OTU data was quantified with the Shannon and Chao1 Indices and significance testing was performed using Mann-Whitney U and a mixed linear model. We described beta diversity with principal components analysis of Euclidean

distances and performed significance testing using PERMANOVA and PERMDISP. Differential abundance analysis was performed with DESeq2 and MaAsLin2. Feature selection was performed with Random Forest, utilizing the ranger package within caret.

Statistical analysis: Statistical analyses were performed in R, CLC Genomic Workbench or GraphPad Prism. In general, $q < 0.05$ after adjustment for multiple comparisons was considered statistically significant.

Supplemental Information

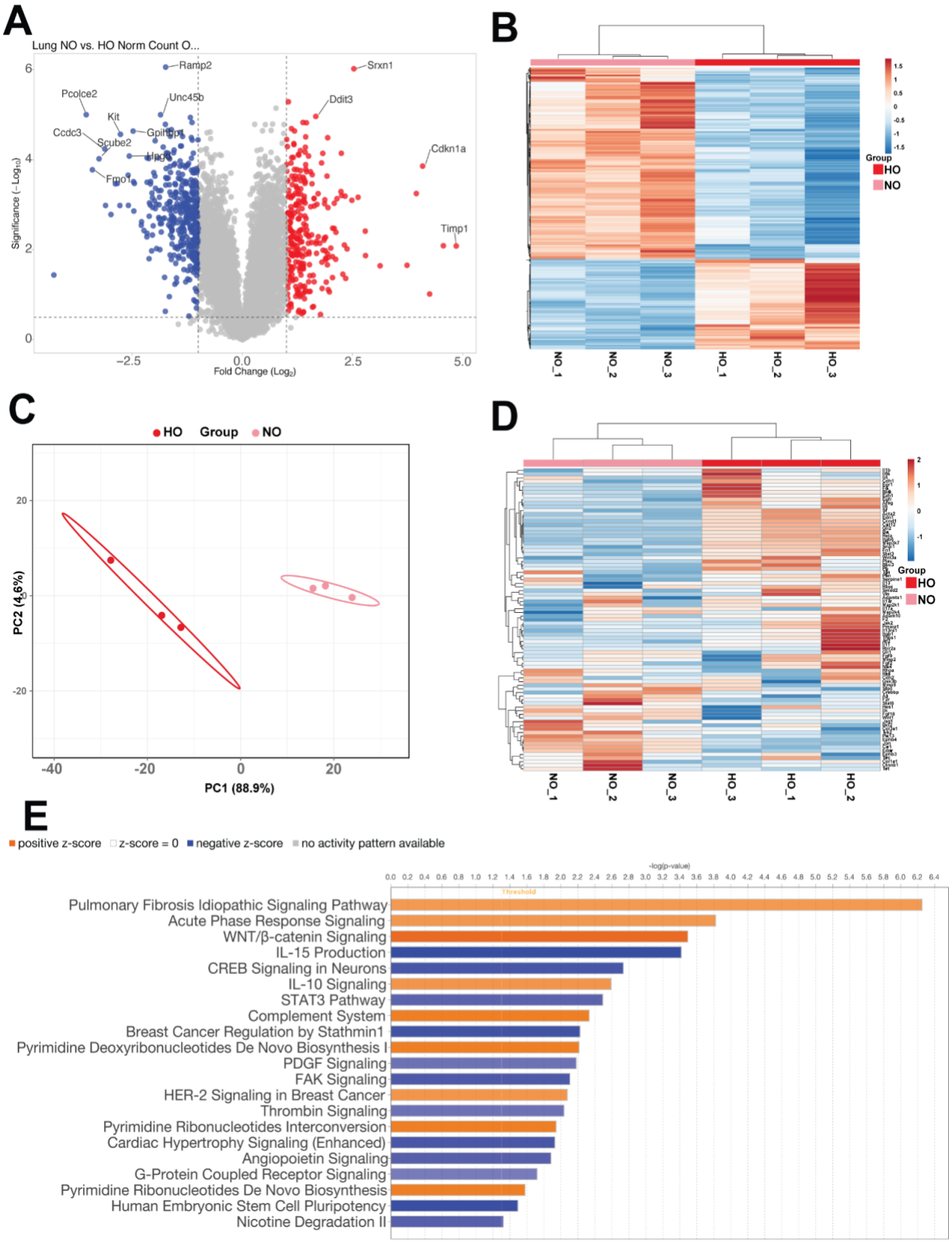

Figure S1. Hyperoxia exposure alters the mouse lung transcriptome.

A) Volcano plot of lung gene expression array showing gene expression altered by hyperoxia exposure. NO, normoxia (pink). HO, hyperoxia (red).
B) Heatmap showing differential gene expression in normoxia versus hyperoxia-exposed mice.
C) Principal components analysis showing differential clustering of mice exposed to normoxia versus hyperoxia. PC, principal component.
D) Heatmap showing differential expression of pulmonary fibrosis-related genes.
E) Differentially expressed pathways in normoxia versus hyperoxia exposure, showing marked increases in fibrosis, acute phase response and WNT/β-catenin-related pathways.

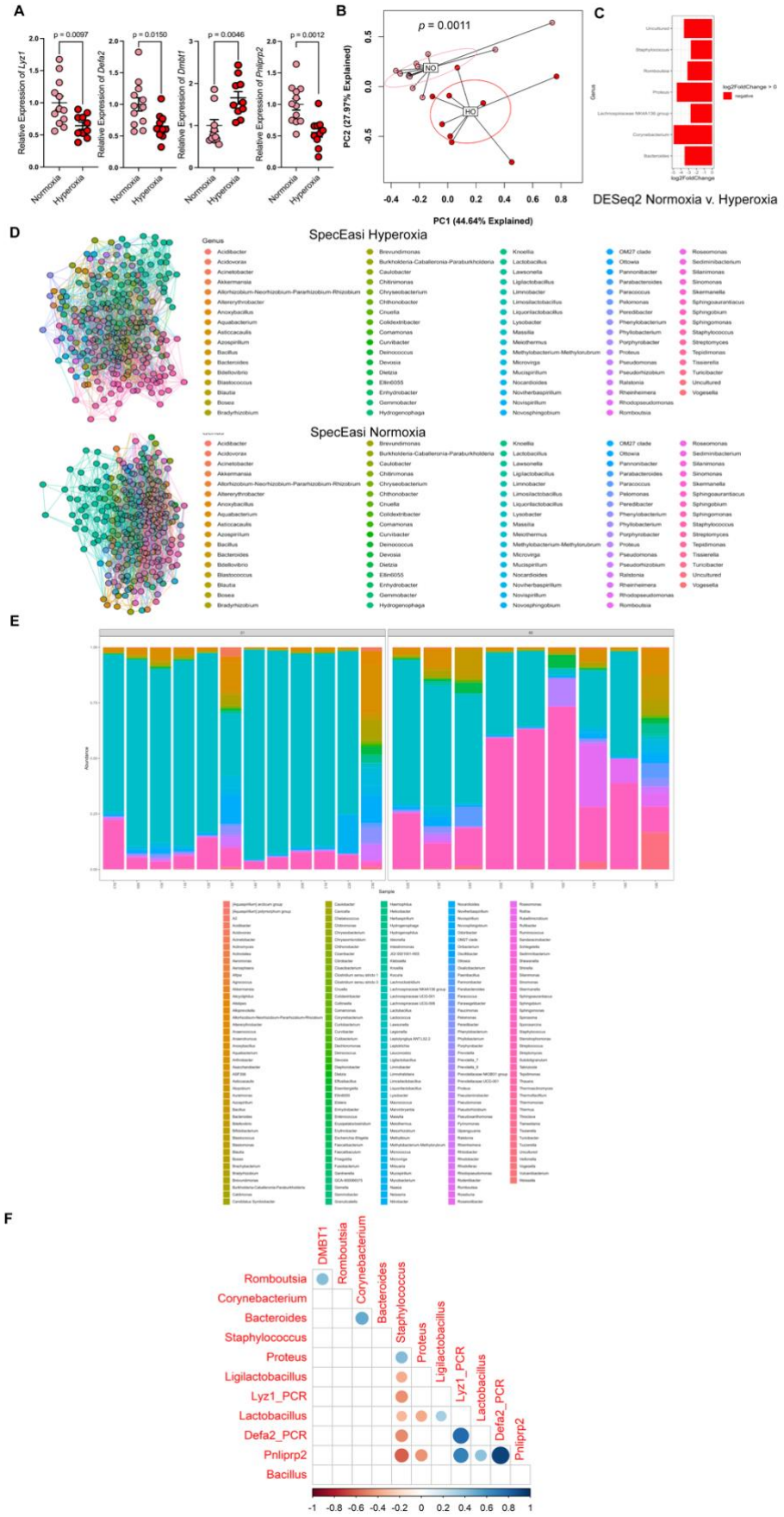
A
p = 0.0097
p = 0.0150
p = 0.0046
p = 0.0012
Relative Expression of Lyz1
Relative Expression of Defa2
Relative Expression of Dmbt1
Relative Expression of Pnliprp2
Normoxia
Hyperoxia
B
p = 0.0011
NO
HO
PC2 (27.97% Explained)
PC1 (44.64% Explained)
C
DESeq2 Normoxia v. Hyperoxia
D
SpecEasi Hyperoxia
SpecEasi Normoxia
E
F
DMBT1
Romboutsia
Corynebacterium
Bacteroides
Staphylococcus
Proteus
Ligilactobacillus
Lyz1_PCR
Lactobacillus
Defa2_PCR
Pnliprp2
Bacillus

Figure S2. Hyperoxia alters the ileal microbiome.

A) Quantitative PCR for a selection of differentially expressed genes showing alterations in expression of antimicrobial peptides and Paneth cell markers.
B) Principal components analysis of Hellinger transformed Euclidian distances, p = 0.0011 pseudo-F = 5.2727 PERMANVOA, p = 1 PERMDISP, showing different global community composition between normoxia- and hyperoxia-exposed neonatal mice. The loading plot for this PCA is shown in Figure 1J.
C) Binomial regression using DESeq2 showing differences at the genera level in normoxia- or hyperoxia-exposed animals.
D) SpiecEasi network analysis of the microbiota of hyperoxia and normoxia exposed mice.
E) Relative abundance at the genera level.
F) Spearman correlation analysis showing association between antimicrobial peptide expression by qPCR and differentially abundant genera.

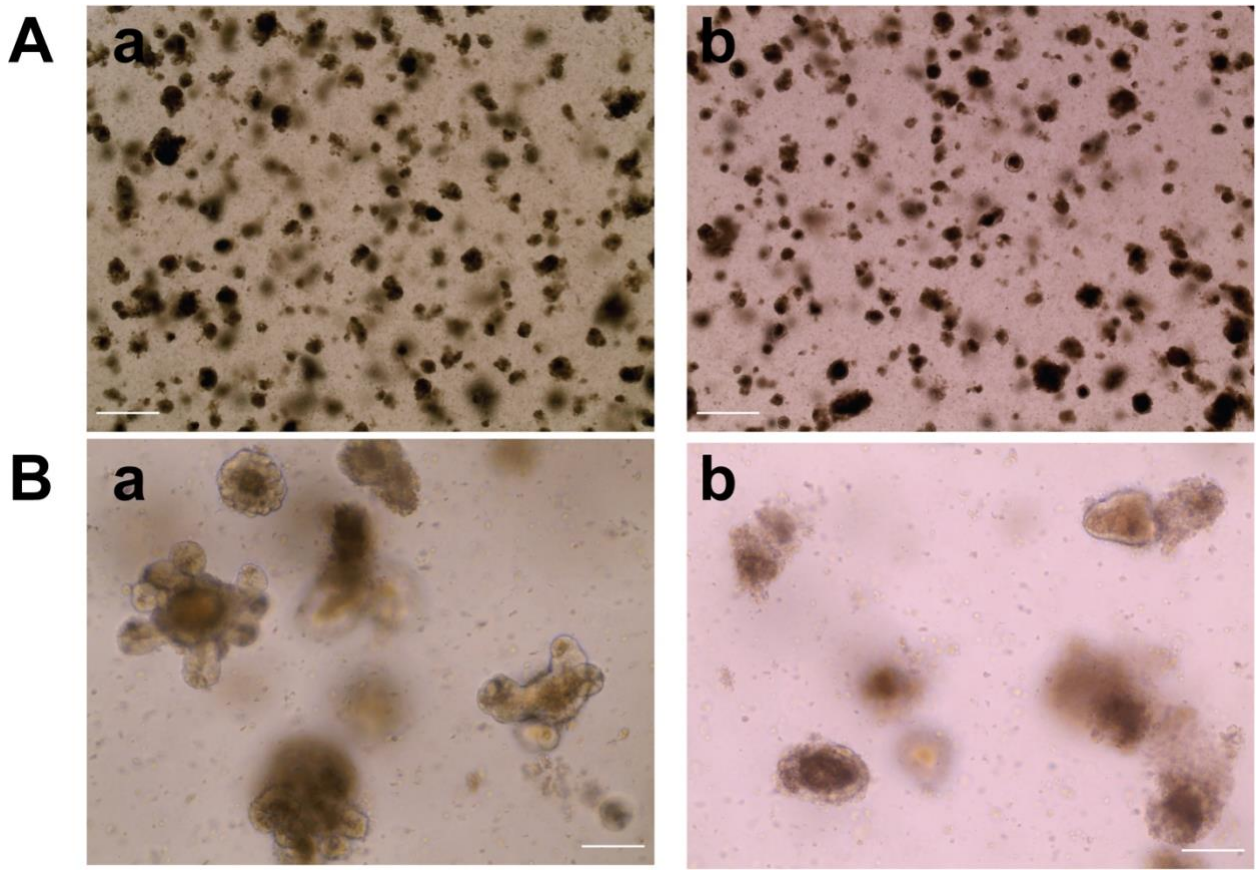

Figure S3. Hyperoxia exposure alters the morphology of intestinal organoids.

A) Visual light microscopy at 4x of intestinal organoids after exposure to (a) normoxia or (b) hyperoxia for 24 h. Scale bar represents 1000 μm.
B) Visual light microscopy and 20x magnification showing less budding and differences in epithelial integrity in (b) hyperoxia exposed organoids. Scale bar represents 200 μm.

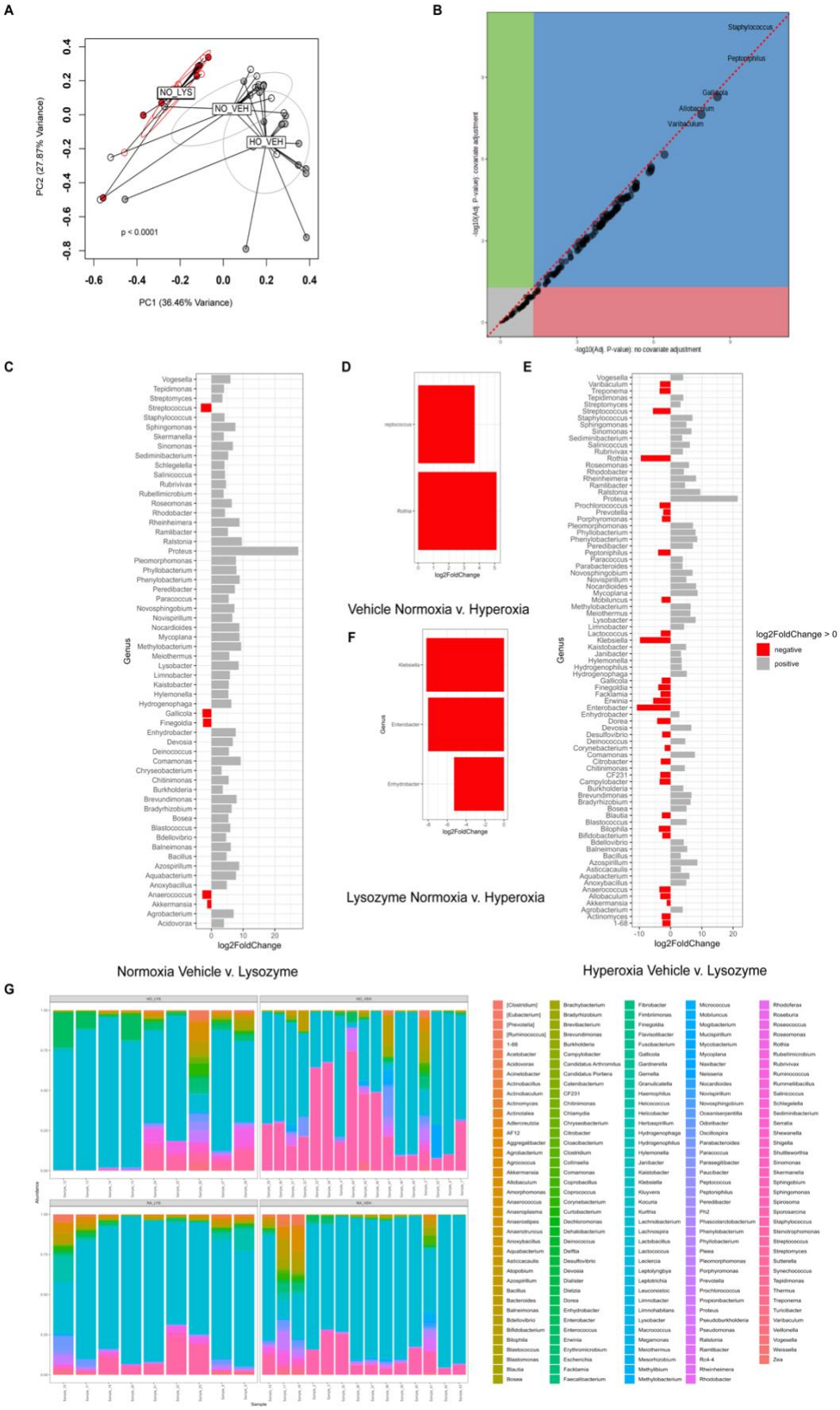
A
NO_LYS
NO_VEH
HO_VEH
p < 0.0001
PC1 (36.46% Variance)
PC2 (27.87% Variance)
B
Staphylococcus
Peptoniphilus
Gallicola
Allobaculum
Varibaculum
-log10(Adj. P-value), covariate adjustment
-log10(Adj. P-value), no covariate adjustment
C
Genus
log2FoldChange
Normoxia Vehicle v. Lysozyme
D
Vehicle Normoxia v. Hyperoxia
E
log2FoldChange > 0
negative
positive
Hyperoxia Vehicle v. Lysozyme
F
Lysozyme Normoxia v. Hyperoxia
G
Abundance
Sample

Figure S4. Lysozyme and hyperoxia alter the ileal microbiome.

A) Principal components analysis of Hellinger transformed Euclidean distances showing significant differences in global community composition, $p < 0.0001$ PERMANOVA, $p = 0.6524$ PERMDISP. That is driven by differences between hyperoxia- and hyperoxia and lysozyme-exposed mice. ($p = 0.0027$, pairwise PERMANOVA hyperoxia versus hyperoxia and lysozyme).
B) MaAsLin 2 (Microbiome Multivariable Associations with Linear Models) showing differences in the intestinal microbiota.
C) Binomial regression showing differences at the genera level in normoxia between vehicle- and lysozyme exposed animals.
D) Binomial regression showing differences between normoxia and hyperoxia vehicle-exposed control animals.
E) Binomial regression showing differences between normoxia and hyperoxia lysozyme-exposed animals.
F) Binomial regression showing differences at the genera level in hyperoxia between vehicle- and lysozyme exposed animals.
G) Relative abundance at the genera level.

Table S1. Paneth cell markers significantly changed in the murine ileum in response to hyperoxia.

Symbol	Fold Change	*P*	Name
Pnliprp2	-5.01959	0.004608	pancreatic lipase-related protein 2
Lyz1	-4.10972	0.012384	lysozyme 1
Dmbt1	-3.8282	0.001136	Deleted In Malignant Brain Tumors 1
Gpx2	-3.32466	0.006985	glutathione peroxidase 2
Reg3g	-2.72808	0.008283	regenerating islet-derived 3 gamma
Guca2b	-2.43296	0.002597	guanylate cyclase activator 2b
Ang4	-2.37332	0.023716	angiogenin
Itln1	-2.10236	0.012832	intelectin 1
Defa1	-1.30565	0.038754	defensin, alpha 1

Table S2. Paneth cell markers significantly changed in the murine intestinal organoids in response to hyperoxia.

Symbol	Fold Change	*P*	Name
Mptx2	-6.10435	2.47E-06	mucosal pentraxin 2
Dmbt1	-5.79307	0.027013	deleted in malignant brain tumors 1
Defa26	-3.80301	1.77E-06	defensin, alpha, 26
Kcnn4	-2.89266	3.81E-05	potassium intermediate/small conductance calcium-activated channel, subfamily N, member 4
Defa23	-2.60226	0.000873	defensin, alpha, 23
Ang4	-2.38428	0.003666	angiogenin, ribonuclease A family, member 4
Defa20	-2.34975	0.013918	defensin, alpha, 20
Defa22	-2.2797	0.023124	defensin, alpha, 22
Defa21	-2.26413	0.027105	defensin, alpha, 21
Defa5	-2.20591	0.029043	defensin, alpha, 5
Wnt3	-1.70433	0.049799	wingless-type MMTV integration site family, member 3
Spink4	-1.65614	0.043295	serine peptidase inhibitor, Kazal type 4
Pnliprp2	-1.63384	0.000914	pancreatic lipase-related protein 2
Dll4	-1.54349	0.040336	delta like canonical Notch ligand 4
Rap1a	1.351647	0.054885	RAS-related protein 1a
Tm4sf20	1.902737	0.001682	transmembrane 4 L six family member 20
Clca1	2.660606	0.000193	chloride channel accessory 1
Guca2b	3.273845	1.09E-06	guanylate cyclase activator 2b (retina)
Guca2a	3.743392	6.98E-09	guanylate cyclase activator 2a (guanylin)

Table S3. Lung inflammation-related genes as compared to normoxia vehicle exposed mice.

	HO VEH vs. NO VEH		HO LYZ vs NO VEH		
Symbol	Fold Change	q	Fold Change	q	Database object name
Ahsg	626.6391	0.005346	21.07616	0.269682	alpha-2-HS-glycoprotein
Csrp3	14.15701	0.000613	-1.133	0.927459	cysteine and glycine-rich protein 3
Mylk3	6.296584	0.000862	-1.28659	0.76882	myosin light chain kinase 3
Il1r2	3.475312	0.025753	1.949132	0.294827	interleukin 1 receptor, type II
Ptger3	2.537922	0.000685	1.6335	0.116541	prostaglandin E receptor 3 (subtype EP3)
Pbk	2.51287	0.017812	1.556554	0.330692	PDZ binding kinase
Ccl6	2.087173	4.42E-06	1.087488	0.740466	chemokine (C-C motif) ligand 6
Clec7a	1.904633	4.27E-06	-1.19229	0.341095	C-type lectin domain family 7, member a
Gpx1	1.797218	2.05E-06	1.19287	0.262587	glutathione peroxidase 1
Ccr2	1.754312	0.026097	1.488087	0.138412	chemokine (C-C motif) receptor 2
Irf5	1.608403	0.014589	1.329064	0.186512	interferon regulatory factor 5
Chid1	1.593086	0.006607	1.357239	0.100582	chitinase domain containing 1
Ndufs4	1.580271	0.000592	1.035841	0.872654	NADH:ubiquinone oxidoreductase core subunit S4
Ctla2a	1.517331	0.00679	1.172581	0.402791	cytotoxic T lymphocyte-associated protein 2 alpha
Stk39	1.513097	0.043299	1.442597	0.074579	serine/threonine kinase 39
Bst1	1.51008	0.035102	1.110652	0.693385	bone marrow stromal cell antigen 1
Dicer1	-1.58638	0.000146	-1.1519	0.361353	dicer 1, ribonuclease type III
F2r	-1.67139	3.58E-05	-1.13661	0.444461	coagulation factor II (thrombin) receptor
Ackr2	-1.69257	0.00167	-1.08879	0.730939	atypical chemokine receptor 2
Kdm6b	-1.6956	2.7E-05	-1.29584	0.071318	KDM1 lysine (K)-specific demethylase 6B
Akna	-1.73878	0.001889	-1.44747	0.052764	AT-hook transcription factor
Cybb	-1.75339	0.001212	-1.36063	0.113292	cytochrome b-245, beta polypeptide
Cdh5	-1.78237	2.99E-05	-1.12635	0.542984	cadherin 5
Adora2a	-2.30738	0.000152	-1.4867	0.113343	adenosine A2a receptor
C1qtnf3	-2.98067	0.006724	-1.60992	0.30865	C1q and tumor necrosis factor related protein 3

Table S4. Genes-related to endothelial cell regulation.

	HO VEH vs. RA VEH		HO LYZ vs RA VEH		
Symbol	FC	q	FC	q	Database object name
Mt3	171.49	0.039911	79.74	0.085312	metallothionein 3
Gata4	3.57	0.001527	1.45	0.48924	GATA binding protein 4
Igf2	2.56	8.07E-05	-1.22	0.560584	insulin-like growth factor 2
Aldh1a2	2.41	2.33E-05	1.19	0.560409	aldehyde dehydrogenase family 1, subfamily A2
Smoc2	2.10	1.53E-05	1.08	0.785722	SPARC related modular calcium binding 2
Gpx1	1.80	2.05E-06	1.19	0.262587	glutathione peroxidase 1
Ccr2	1.75	0.026097	1.49	0.138412	chemokine (C-C motif) receptor 2
Itgb1bp1	1.69	0.000516	1.25	0.216524	integrin beta 1 binding protein 1
Nr4a1	1.67	0.034821	-1.17	0.62015	nuclear receptor subfamily 4, group A, member 1
Mydgf	1.60	0.000569	1.32	0.060535	myeloid derived growth factor
Fgf18	1.50	0.013835	1.03	0.916387	fibroblast growth factor 18
Stard13	-1.50	0.025186	-1.04	0.9001	StAR-related lipid transfer (START) domain containing 13
Jup	-1.50	0.003187	-1.18	0.324177	junction plakoglobin
Cxcl12	-1.50	0.01231	1.01	0.985026	chemokine (C-X-C motif) ligand 12
Paxip1	-1.55	0.005012	-1.24	0.22634	PAX interacting (with transcription-activation domain) protein 1
Crkl	-1.56	0.003138	-1.03	0.909193	v-crk avian sarcoma virus CT10 oncogene homolog-like
Dicer1	-1.59	0.000146	-1.15	0.361353	dicer 1, ribonuclease type III
Mecp2	-1.59	0.000473	-1.08	0.682247	methyl CpG binding protein 2
Jag1	-1.59	0.002791	1.14	0.53448	jagged 1
Flt1	-1.59	0.008216	1.03	0.929469	FMS-like tyrosine kinase 1
Ece1	-1.64	1.62E-05	-1.19	0.207628	endothelin converting enzyme 1
Fzd4	-1.67	0.034973	1.25	0.431742	frizzled class receptor 4
Atoh8	-1.68	0.001662	-1.39	0.06783	atonal bHLH transcription factor 8
Kdm6b	-1.70	2.7E-05	-1.30	0.071318	KDM1 lysine (K)-specific demethylase 6B
Ptprm	-1.71	2.19E-05	-1.06	0.778646	protein tyrosine phosphatase, receptor type, M
Sp1	-1.72	4.56E-05	-1.20	0.26853	trans-acting transcription factor 1
Cdh5	-1.78	2.99E-05	-1.13	0.542984	cadherin 5
Pecam1	-1.79	2.22E-05	-1.23	0.220446	platelet/endothelial cell adhesion molecule 1
Pde4d	-1.81	0.000142	-1.33	0.104711	phosphodiesterase 4D, cAMP specific
Flt4	-1.87	1.53E-06	-1.18	0.332498	FMS-like tyrosine kinase 4
Il6ra	-2.55	4E-05	-1.56	0.084073	interleukin 6 receptor, alpha
Lgals12	-5.58	0.043358	1.26	0.832064	lectin, galactose binding, soluble 12
Fgf2	-6.15	0.047026	2.32	0.342984	fibroblast growth factor 2

Table S5. Genes with opposite regulation associated with lysozyme supplementation.

	HO_VEH vs. RA_VEH FC	HO_VEH vs. RA_VEH q	HO_LYZ vs. RA_VEH FC	HO_LYZ vs. RA_VEH q	HO_LYZ vs. HO_VEH FC	HO_LYZ vs. HO_VEH q	Database object name
Sln	13.69	0.000426	-11.55	0.003672	-158.08	2.94E-10	sarcolipin
Myl7	6.38	0.001178	-4.37	0.013565	-27.89	4.11E-09	myosin, light polypeptide 7, regulatory
Hba-a2	4.21	0.000184	-2.45	0.032445	-10.30	1.53E-09	hemoglobin alpha, adult chain 2
Hbb-bt	4.16	0.000119	-2.83	0.007483	-11.79	2.44E-11	hemoglobin, beta adult t chain
Hba-a1	3.87	0.000579	-2.65	0.019222	-10.22	2.74E-09	hemoglobin alpha, adult chain 1
Snca	3.63	0.000852	-2.38	0.038694	-8.65	2.51E-08	synuclein, alpha
Alas2	3.61	0.000565	-3.21	0.001881	-11.59	2.27E-11	aminolevulinic acid synthase 2, erythroid
Hbb-bs	2.97	0.016819	-4.08	0.000942	-12.09	4.03E-09	
Slc4a1	2.47	0.008169	-2.32	0.015472	-5.74	1.53E-07	solute carrier family 4 (anion exchanger), member 1
Cpe	1.74	0.000235	-1.75	0.000201	-3.03	5.23E-14	carboxypeptidase E
Igfbp5	1.51	0.041052	-1.82	0.001169	-2.75	4.24E-08	insulin-like growth factor binding protein 5
mt-Rnr2	1.51	0.016924	-1.60	0.004611	-2.41	5.45E-08	mitochondrially encoded 16S rRNA
S100a1	1.39	0.036962	-1.41	0.023687	-1.97	7.7E-06	S100 calcium binding protein A1
Glg1	-1.53	0.034846	1.86	0.000484	2.84	6.73E-09	golgi apparatus protein 1
Abhd2	-1.99	0.003723	1.79	0.014075	3.56	3.21E-08	abhydrolase domain containing 2

Supplemental References

1. Kilkenny, C., Browne, W.J., Cuthill, I.C., Emerson, M., and Altman, D.G. (20*10*). Improving bioscience research reporting: the ARRIVE guidelines for reporting animal research.
2. Willis, K.A., Siefker, D.T., Aziz, M.M., White, C.T., Mussarat, N., Gomes, C.K., Bajwa, A., Pierre, J.F., Cormier, S.A., and Talati, A.J. (201*9*). Perinatal maternal antibiotic exposure augments lung injury in offspring in experimental bronchopulmonary dysplasia. American Journal of Physiology - Lung Cellular and Molecular Physiology *3*, 21. 10.1152/ajplung.00561.2018.
3. Nardiello, C., Mižíková, I., Silva, D.M., Ruiz-Camp, J., Mayer, K., Vadász, I., Herold, S., Seeger, W., and Morty, R.E. (2017). Standardisation of oxygen exposure in the development of mouse models for bronchopulmonary dysplasia. Disease models & mechanisms 10, 185–196. 10.1242/dmm.027086.
4. Wang, W., Yan, T., Guo, W., Niu, J., Zhao, Z., Sun, K., Zhang, H., Yu, Y., and Ren, T. (2021). Constitutive GLI1 expression in chondrosarcoma is regulated by major vault protein via mTOR/S6K1 signaling cascade. Cell Death Differ *28*, 2221–2237. 10.1038/s41418-021-00749-4.
5. Metsalu, T., and Vilo, J. (2015). ClustVis: a web tool for visualizing clustering of multivariate data using Principal Component Analysis and heatmap. Nucleic Acids Res *43*, W566–W570. 10.1093/nar/gkv468.
6. Baker, J.M., Hinkle, K.J., McDonald, R.A., Brown, C.A., Falkowski, N.R., Huffnagle, G.B., and Dickson, R.P. (2021). Whole lung tissue is the preferred sampling method for amplicon-based characterization of murine lung microbiota. Microbiome 9, 99. 10.1186/s40168-021-01055-4.